Optimal Purification of a Spin Ensemble by Quantum-Algorithmic Feedback

Daniel M. Jackson,[1,§] Urs Haeusler,[1,§] Leon Zaporski,[1] Jonathan H. Bodey,[1] Noah Shofer,[1] Edmund Clarke,[2] Maxime Hugues,[3] Mete Atatüre,[1,*] Claire Le Gall,[1,†] and Dorian A. Gangloff[1‡,‖]

[1]*Cavendish Laboratory, University of Cambridge, JJ Thomson Avenue, Cambridge CB3 0HE, United Kingdom*

[2]*EPSRC National Epitaxy Facility, University of Sheffield, Broad Lane, Sheffield S3 7HQ, United Kingdom*

[3]*Université Côte d'Azur, CNRS, CRHEA, rue Bernard Gregory, 06560 Valbonne, France*

(Received 29 October 2021; revised 7 March 2022; accepted 10 June 2022; published 21 July 2022)

Purifying a high-temperature ensemble of quantum particles toward a known state is a key requirement to exploit quantum many-body effects. An alternative to passive cooling, which brings a system to its ground state, is active feedback, which stabilizes the system at a chosen target state. This alternative, if realized, offers additional control capabilities for the design of quantum states. Here we present a feedback algorithm applied to a quantum system, which is capable of stabilizing the collective state of an ensemble from its maximum entropy state to the limit of single quantum fluctuations. Our algorithmic approach maximizes the rate of state purification given the system's physical constants; thus it remains the optimal feedback approach even in the presence of dissipation and disorder. We test experimentally the robustness of this feedback on the highly inhomogeneous nuclear-spin ensemble of a semiconductor quantum dot, reducing nuclear-spin fluctuations 83-fold, down to 5.7(2) spin macrostates. Simulations demonstrate that without system-specific inhomogeneities, our algorithm can purify the system down to single-spin fluctuations. Further, we exploit our algorithmic approach to tailor nontrivial nuclear-spin distributions that go beyond simple polarization, including weighted bimodality and latticed multistability. This control is a precursor toward quantum-correlated macrostates, which an extended version of our algorithm could generate in homogeneous systems.

DOI: 10.1103/PhysRevX.12.031014

Subject Areas: Condensed Matter Physics
Quantum Physics
Quantum Information

I. INTRODUCTION

A controllable system of many interacting quantum objects hosts a phenomenally large Hilbert space which can serve as a versatile resource for both technological [1] and fundamental physics applications [2]. These range from realizing multiqubit registers for quantum information processing [3–6] and storage [7–9] to exploring collective phenomena such as superradiance [10,11] and discrete time crystal formation [12,13]. Leveraging this resource requires reducing the ambient-condition entropy of such systems from that of a highly mixed thermal state to that of a pure state that reveals their quantum properties. Advances in cooling techniques have been transformative in achieving this goal in multiple physical platforms. Laser cooling of atomic gases and single trapped atoms [14]—including Doppler, motional sideband-resolved, and spin-assisted Raman-based techniques [15–18]—as well as sideband cooling in electromechanical [19,20], optomechanical [21], and superconducting qubit systems [22] have been the trailblazers in this quest. In contrast to direct cooling, active stabilization at a target quantum state, in principle, also allows purification of a many-body state. Such an approach further enables the programmable preparation of nonequilibrium states and can be used to engineer designer ensemble distributions with varied many-body correlations. While the complex dynamics of highly degenerate many-body systems make stabilizing a single *microstate* very

*Corresponding author.
ma424@cam.ac.uk
†Corresponding author.
cl538@cam.ac.uk
‡Corresponding author.
dorian.gangloff@eng.ox.ac.uk.
§These authors contributed equally to this work.
‖Present address: Department of Engineering Science, University of Oxford, Parks Road, Oxford OX1 3PJ, United Kingdom.

challenging, techniques to purify toward a single *macrostate* remain highly desirable. Toward this end, the field of optimal quantum feedback control has developed an extensive toolbox [23] that can be exploited for quantum state engineering.

Feedback on a system comprises three elements [24]: sensor, controller, and actuator. The sensor detects the current state of the system, a controller processes this information and tells the actuator how to correct the system toward a target state. In the case of quantum feedback, the control loop leverages quantum objects to enable sensing and actuation at the fundamental level of single quanta. A first example is measurement-based quantum feedback [25], which employs weak measurement of quantum observables to obtain classical information that is then processed by external electronics and used to control the actuator. This approach has been used for stabilizing single qubit states [26], squeezed mechanical states [27], photonic Fock states [28], and mesoscopic spin squeezing [29], but limitations arise from measurement backaction and the rate-limiting classical electronics required. Going further, coherent quantum feedback [30] overcomes these limitations by feeding quantum information directly from the sensor to the actuator without a measurement step. This enables autonomous stabilization, and has been implemented in photonic [31] and few-spin [32,33] systems. Extending it to complex mesoscopic systems remains an open direction and, in this regime, a central spin coupled to a dense ensemble of nuclear spins serves as an ideal prototype. Techniques to stabilize the macrostate of this spin ensemble via the central spin, even far from the optimum of a single macrostate, have been a game changer: in gate-defined quantum dots (QDs), coherent sensing via an electronic proxy, combined with nuclear-spin pumping, achieved a reduced-fluctuation, correlated state of two nuclear-spin baths [34], while in optically active QDs autonomous feedback has opened a window into the many-body physics of the nuclei [35–37]. Preparation of the large spin ensemble into a single macrostate, by achieving single-quanta level of control, remains an outstanding challenge.

In this work, we design an autonomous, time-sequenced feedback algorithm capable of stabilizing and engineering a mesoscopic spin system to within single-spin fluctuations of a target macrostate. Through simulation, we verify this capability for an idealized central spin system. Since our algorithm optimizes the use of the available coherence during gate operations, it constitutes the optimal feedback even in nonideal systems. To demonstrate this experimentally, we apply our optimum feedback control to the highly inhomogeneous, noisy nuclear-spin ensemble of an optically active QD. This requires the deterministic correction of deviations from a target state at the level of a single quantum, which we achieve by exploiting the recent advances of sensing [38] and coherent control [37] of single collective excitations in a nuclear ensemble—nuclear magnons. Leveraging the coherence of these sensing and control processes, the central electron acts as both the sensor and actuator in a feedback loop which, followed by a spin initialization step via optical pumping, removes entropy from the spin ensemble. We demonstrate a reduction by 2 orders of magnitude in the thermal fluctuations of the spin ensemble, only a factor of 3 away from the fundamental quantum limit of single-spin fluctuations. Within the broader context of autonomous feedback [34,36,39,40], our algorithmic approach allows an improvement of a factor 4 over the state of the art [37]. Such performance is a testament to the robustness and applicability of this algorithmic approach which extends to highly inhomogeneous, real-world systems. Further, the control afforded by the use of quantum gates at each step allows us to sculpt the feedback to generate tailored nuclear-spin distributions of the ensemble. Going beyond this, we propose a simple extension of our algorithm to allow the proliferation of quantum coherences of the ensemble that are otherwise destroyed by optical pumping.

II. RESULTS

A. Three-step feedback algorithm

The generality of our feedback algorithm allows it to be applied to a general central-spin [41] or central-boson [42] system [Fig. 1(a)]. We present each feedback step in general terms and realize their implementation with the physical system of a QD electron spin interfaced to $N \approx 50\,000$ nuclear spins [43]. We parametrize this spin system by its collective state consisting of a total angular momentum I and a polarization along the quantization axis $I_z \in [-I, I]$. In the case of a homogeneous one-to-all electron-nuclear coupling, the electron can change I_z via single collective excitations, while I is protected by symmetry [44]. Thus the feedback actuated by the electron corrects one nuclear-spin deviation at a time, and in doing so, purifies the state of the nuclear-spin system. An external magnetic field of 3.5 T along the z-direction Zeeman splits the electron spin, which we control with all-optical electron-spin resonance (ESR) allowing for fast multiaxis control [45] (Appendix A 1). The system Hamiltonian, expressed in a frame rotating at the ESR drive frequency ω, is given by

$$H_0 = \delta S_z + \Omega S_x + \omega_n I_z + A_c S_z I_z + A_{nc} S_z I_x, \quad (1)$$

where S_i and I_i are electron- and nuclear-spin operators, respectively. The ESR detuning, Rabi frequency, and nuclear Zeeman frequency are denoted $\delta = \omega_e - \omega$, Ω, and ω_n, respectively. The electron-nuclear coupling is enabled by the collinear (A_c) and the noncollinear (A_{nc}) constituents of the hyperfine constant. The collinear hyperfine term $A_c S_z I_z$ facilitates sensing by the electron since the

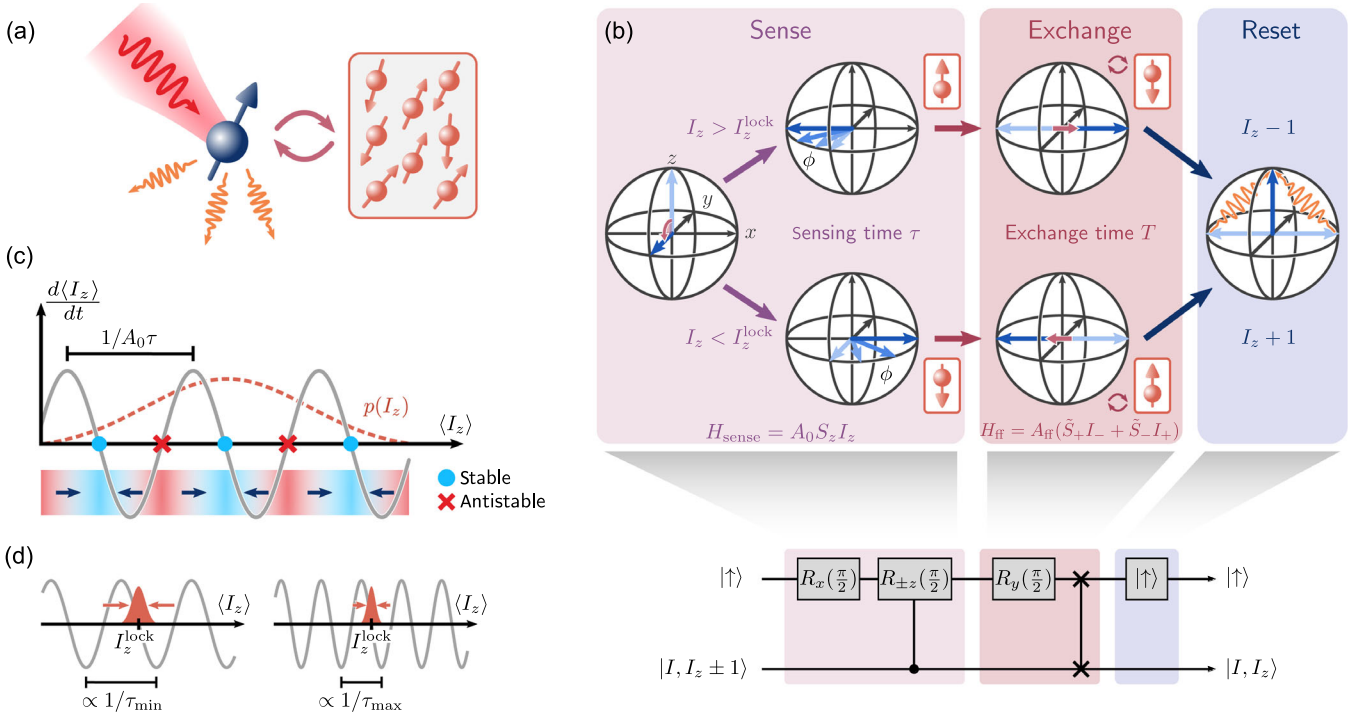

FIG. 1. Quantum-algorithmic feedback. (a) Pulsed control (red shading) of a central spin (blue), homogeneously coupled to a spin ensemble (red), can purify the state of the system, removing entropy via spontaneous scattering (orange). (b) The feedback algorithm. Top: Bloch sphere representation of the electron-spin evolution during one algorithm cycle. The upper (lower) path represents the case of a positive (negative) ΔI_z. Bottom: quantum circuit representation of the feedback algorithm operating in the single-spin limit. The upper and lower rails represent, respectively, the central spin and the $\{|I, I_z \pm 1\rangle, |I, I_z\rangle\}$ states of the spin ensemble. (c) The rate of change $d\langle I_z\rangle/dt$ as a function of $\langle I_z\rangle$ (gray curve) on a coarse-grained evolution time $t \gg \tau + T$, displaying multiple (anti)stable setpoints arising from the $1/A_0\tau$ periodicity of the sensing gate. The red dashed curve represents the initial thermal probability distribution. (d) To purify an initially broad distribution (left, red shaded area) to a narrow single mode centered around $I_z^{\rm lock}$ (right, red shaded area), we increase the sensing time dynamically from $\tau_{\rm min}$ to $\tau_{\rm max}$.

ESR frequency is modified by a mean Overhauser field $A_c I_z$, and sensing of a single nuclear spin flip was recently shown in this system [38]. The electron is also the actuator thanks to the electron-nuclear exchange coupling enabled by the nuclear quadrupolar interaction, which reduces to a noncollinear hyperfine interaction $A_{\rm nc} S_z I_x$ [46,47]. This coupling enables the injection of a single nuclear magnon [37], with a rate $f(I, I_z)A_{\rm nc}$ that depends on the ensemble's total angular momentum I and its polarization I_z via the enhancement factor $f(I, I_z) \sim \mathcal{O}(\sqrt{N})$ [10,48].

During feedback we employ sensing and actuation as sequential quantum gates. This allows us to leverage the available coherence for maximum fidelity gate operations at each step. With sensing and injection possible at the fundamental level of single quanta (nuclear spin flips) in the ensemble, the ideal feedback limit can be reached: detecting single-unit deviations from a target macrostate $I_z^{\rm lock}$ and correcting them with exactly one unit. We first consider evolution during the feedback in the ideal, fully unitary case, except where dissipation is deliberately introduced. The feedback algorithm proceeds through the following three steps, which we visualize on the sequence of Bloch spheres and the corresponding quantum circuit in Fig. 1(b).

(1) *Sense.*—A straightforward sensing mechanism for macrostate I_z is a linear energy shift on the central spin: $H_{\rm sense} = A_0 S_z I_z$, with A_0 as a general coupling constant. The most efficient way to measure this energy shift is via Ramsey interferometry [49], with steps as follows. (i) The central spin starts spin $|\uparrow\rangle$. (ii) An $R_x(\pi/2)$ rotation places it in a coherent spin superposition in the Bloch equator. (iii) A free evolution time τ under $H_{\rm sense}$ causes precession of the Bloch vector, whose projection along the x direction will be the error signal for a deviation $\Delta I_z = I_z - I_z^{\rm lock}$ from a target macrostate $I_z^{\rm lock}$: $\langle S_x\rangle = -\frac{1}{2}\sin(2\pi A_0 \Delta I_z \tau)$, which for a single spin flip $\Delta I_z = 1$ reaches a maximum at $\tau = 1/4A_0$. In the quantum circuit, this optimum evolution time corresponds to an $R_{\pm z}(\pi/2)$ rotation conditional on the state of the spin system. [(iv), optional] A final rotation $R_y(\pi/2)$ may be required to convert this signal to an $\langle S_z\rangle$ polarization, depending on the type of actuator gate that follows. Our example QD

system, where $A_0 = A_c$, implements this sensing procedure naturally with $H_{\text{sense}} = (\delta + A_c I_z + A_{nc} I_x) S_z$. The ESR drive detuning $\delta \equiv -A_c I_z^{\text{lock}}$ determines the primary setpoint of the algorithm which feeds back on fluctuations $\Delta I_z = I_z - I_z^{\text{lock}}$. The transverse field $A_{nc} I_x$, which oscillates at ω_n, contributes to sensing errors up to $\sqrt{N} A_{nc}/A_c$, but can in principle be circumvented by an appropriate choice of B field or τ (Appendix E 3 b); it is an important consideration in determining the ultimate feedback limit.

(2) *Actuate.*—Evolution under a flip-flop Hamiltonian $H_{\text{ff}} = A_{\text{ff}}(\tilde{S}_+ I_- + \tilde{S}_- I_+)$ for a time T converts the error signal $\langle \tilde{S}_z \rangle = -\frac{1}{2}\sin(2\pi A_0 I_z \tau)$ into a spin flip toward the target macrostate. Here $\tilde{S}$ represents a simple basis rotation, reflecting the fact that some physical systems produce collinear flip-flop terms, where $\tilde{S}_z = S_z$ [and the final $R_y(\pi/2)$ is then required in the sensing step to make the error signal proportional to S_z], and others like our QD platform yield noncollinear terms, where $\tilde{S}_z = S_x$. Evolution under H_{ff} for a time $T = 1/2f(I, I_z)A_{\text{ff}}$ performs a SWAP operation between the central spin and a single collective spin excitation. No measurement is made between steps 1 and 2, meaning the operation thus far is autonomous and reversible. In our QD system, we engineer the flip-flop Hamiltonian from the $A_{nc} S_z I_x$ term by driving the central spin at Hartmann-Hahn (HH) resonance [45,50], $\Omega \approx \omega_n$, yielding $\tilde{H}_{\text{ff}} = \Omega \tilde{S}_z + \omega_n I_z - (A_{nc}/4)(\tilde{S}_+ I_- + \tilde{S}_- I_+)$ [51], where $A_{\text{ff}} = A_{nc}/4$.

(3) *Reset.*—Up until this point the quantum algorithm has corrected deviations from the setpoint, $\Delta I_z = I_z - I_z^{\text{lock}}$, by flipping a single spin within the ensemble entirely coherently, and therefore reversibly. To purify the spin ensemble further, we perform an irreversible reset operation on the central spin. In our QD system, this reset step is achieved by exciting the central spin to the charged exciton (trion) manifold with an optical pulse that incoherently pumps and repolarizes the electron to state $|\uparrow\rangle$ with $> 98\%$ probability. In doing so, we effectively transfer entropy from the spin ensemble to the photonic bath via the central spin, in analogy with heat-bath algorithmic cooling [52].

Applying the above algorithm repeatedly increases the purity of the spin bath and can, in principle, prepare a single I_z macrostate to within single-spin fluctuations. In practice, nuclear-spin diffusion mechanisms, which are external to the feedback steps above, will compete with the feedback loop and limit the purity of the steady-state preparation. The approach to equilibrium under these competing effects can be gleaned qualitatively from a simple semiclassical rate equation governing the evolution of the mean value $\langle I_z \rangle$ [40,47] (Appendix D), valid over a coarse-grained evolution time $t \gg \tau + T$:

$$\frac{d\langle I_z \rangle}{dt} = \frac{-\sin[2\pi A_0 \langle \Delta I_z \rangle \tau]}{\tau + 1/2A_{\text{ff}}} - \Gamma_d \langle I_z \rangle. \tag{2}$$

The first term is the rate at which the sensing, actuate, and reset gates together change $\langle I_z \rangle$ as a function of $\langle I_z \rangle$—it is the nonlinear dynamical function defining the feedback dynamics. The second term is a standard relaxation term capturing all spin diffusion mechanisms that relax a nonzero polarization $\langle I_z \rangle$ at a rate Γ_d. We see that in the low diffusion regime $\Gamma_d \ll A_{\text{ff}}/(1 + 2A_{\text{ff}}\tau)$, setting the sensing time to $\tau = 1/4A_0$ programs the feedback at its global optimal $T_0\, d\langle I_z \rangle/dt = -1$ for $\langle \Delta I_z \rangle = 1$, where $T_0 = 1/4A_0 + 1/2A_{\text{ff}}$—i.e., a fluctuation of one unit is fully corrected within a single algorithm cycle.

Figure 1(c) shows the curve described by Eq. (2), on which we have highlighted the stable points of the feedback dynamics defined by a zero crossing and a negative slope of $d\langle I_z \rangle/dt$. A key feature is the existence of multiple stable points split by $1/A_0\tau$ in the $\langle I_z \rangle$ phase space. This arises intuitively from the 2π-periodic temporal phase acquisition during sensing, meaning the feedback does not distinguish between points in the phase space where $A_0 \Delta I_z \tau \in \mathbb{Z}$. The splitting between stable points is effectively the capture range for each stable point in the I_z phase space—all fluctuations within this capture range are shepherded back toward the same stable point. Polarization fluctuations are described fully by the probability distribution of macrostates I_z: $p(I_z) = \langle I_z | \text{Tr}_e(\rho) | I_z \rangle$, where we trace the full system's density matrix ρ over the central spin (e). In this picture, a physical system with an initial state at large temperature (that is, all microstates are equiprobable) exhibits a broad initial $p(I_z)$ distribution [Fig. 1(c)], with variance $\langle \Delta I_z^2 \rangle \sim N$. Adapting the feedback capture range to the system's initial state is thus critical to lock the system to a desired stable point I_z^{lock}; a capture range narrower than the typical width of $p(I_z)$ splits the ensemble into multiple stabilized modes. However, extending the capture range by shortening the sensing duration results in a reduced feedback strength, as per Eq. (2). To resolve this tension, we vary the sensing time dynamically, changing it from sequence to sequence, such that the first in the series $\tau_{\text{min}} \sim 1/4A_0\sqrt{N}$ has a capture range sufficient for a thermal state and the last in the series $\tau_{\text{max}} \sim 1/4A_0$ optimally corrects single-spin fluctuations [Fig. 1(d)].

B. Ultranarrow QD nuclear ensemble

Figure 2(a) shows the full control sequence we employ in our QD system for feedback, where we have $\sim 15\ \mu$s of nuclear-state purification, consisting of 44 elementary units of the algorithm—this sequence is used throughout this work. Between each unit, we increase the sensing time linearly from $\tau_{\text{min}} = 30$ ns to $\tau_{\text{max}} \leq 150$ ns, and

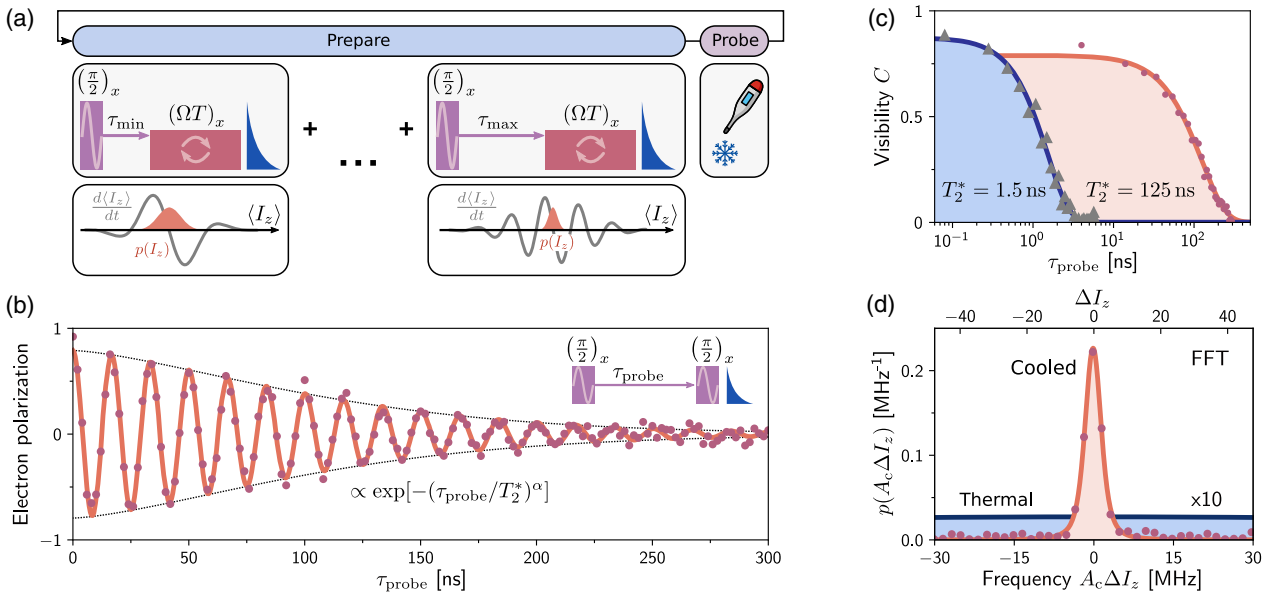

FIG. 2. Optimal feedback algorithm. (a) Feedback control sequence. We use 44 elementary blocks of the algorithm. Each block has an $R_x(\pi/2)$ rotation to initiate sensing (purple), an $R_x(\Omega T)$ pulse to actuate a spin flip via a HH resonance (red), and optical pumping for electron reset (blue). The sensing time is increased linearly over the 44 blocks from $\tau_{\min}$ to $\tau_{\max}$, resulting in the schematic feedback curves (gray) beneath. (b) Electronic FID under optimal feedback. We alternate ∼15 μs of feedback—where $\tau_{\min} = 30$ ns, $\tau_{\max} = 98$ ns, $\Omega = 29$ MHz, and $T = 86$ ns—with ∼2 μs of probing $p(\Delta I_z)$ via Ramsey interferometry (inset), yielding a 60 kHz repetition rate for single shots of the experiment. Each data point is an ensemble average measurement integrated for 2 sec. The purple circles are the FID $\langle S_z(\tau_{\text{probe}}) \rangle$ as a function of Ramsey delay τ_{probe}. The FID oscillates at a frequency $\omega_{\text{serr}} = 60$ MHz set by the phase, $2\pi\omega_{\text{serr}}\tau_{\text{probe}}$, which we add to the second Ramsey gate to make the process of fitting the envelope robust against small systematic detunings. The red curve is a phenomenological fit to a cosine with envelope $C(\tau_{\text{probe}}) = \exp[-(\tau_{\text{probe}}/T_2^*)^\alpha]$ (dotted curve), where $T_2^* = 125(4)$ ns and $\alpha = 1.46(9)$. (c) Triangles (circles) are the FID envelopes resulting from a nuclear-spin ensemble without (with) the application of our optimized feedback algorithm. Fitting these data with the blue and red $C(\tau_{\text{probe}})$ curves yields $T_2^* = 1.52(5)$ ns, $\alpha = 1.60(12)$ and $T_2^* = 125(4)$ ns, $\alpha = 1.46(9)$, respectively. (d) Fourier transform of data (circles) and FID envelopes (curves) from Fig. 2(c), yielding explicitly the probability distribution $p(A_c \Delta I_z)$ for the purified (thermal) ensemble shown in red (blue).

Fig. 2(a) shows the effective feedback curves at each step. In contrast to Fig. 1 the $d\langle I_z \rangle/dt$ curves have an envelope function corresponding to the finite bandwidth of our feedback implementation. This width is dictated by the electron-nuclear coupling rate during actuation $\frac{1}{4}A_{\text{nc}}\sqrt{N/2} \sim 4$ MHz, which restricts efficient polarization transfer to ΔI_z fluctuations satisfying $\sqrt{\omega_n^2 + (A_c \Delta I_z)^2} - \omega_n \lesssim 4$ MHz, thereby defining a full bandwidth $|A_c \Delta I_z| \approx 30$ MHz. The preparation step is followed by a probe step to determine the characteristic width of the probability distribution $p(\Delta I_z)$, which measures how close the prepared system is to an ideal single macrostate I_z^{lock}. To measure $p(\Delta I_z)$, we again use the electron's sensing capability; specifically, we use Ramsey interferometry [Fig. 2(b)]. An $R_x(\pi/2)$ gate applied to an initialized electron spin followed by a wait time τ_{probe} leads to phase accumulation which senses the mean field $A_c I_z$. This phase is mapped to electron population $\rho_{\uparrow\uparrow}$ with a final $R_x(\pi/2)$ gate. We use a second Ramsey measurement but with a final $R_{-x}(\pi/2)$ gate to obtain a calibrated measurement of electron polarization (Appendix A 2). By repeating $\mathcal{O}(10^5)$ such pump-probe measurements over a few seconds, we obtain the ensemble average electronic evolution over $p(A_c \Delta I_z)$, namely the free-induction decay (FID) of the electronic spin. Figure 2(b) shows the electron polarization as a function of the probe time τ_{probe}, that is, the FID following preparation with the feedback sequence of Fig. 2(a), with visible coherence extending to 300 ns.

Fitting the FID with a stretched exponential envelope $C(\tau_{\text{probe}}) = \exp[-(\tau_{\text{probe}}/T_2^*)^\alpha]$, where $\alpha > 0$ is a free parameter, we find an electronic coherence time $T_2^* = 125(4)$ ns [Fig. 2(c), red curve]. This is an improvement by a factor of 83 relative to the FID taken with a probe measurement of the system without a preparation step. Indeed, a probe measurement of the thermal ensemble at the ambient temperature for our experiments (4 K) yields a coherence time $T_2^* = 1.52(5)$ ns [Fig. 2(c), blue curve]. Our experiments on the purified state are conducted by probing for a few microseconds after ∼15 μs of state preparation; each pump-probe unit is repeated 10^6–10^7 times for each data point. At all times, the ensemble is at steady state as nuclear-spin relaxation is negligible on these

microsecond timescales. Previous measurements on this device indicate that, when prepared from thermal equilibrium, spin fluctuations reach their purified steady state on a millisecond timescale, and when subsequently left to relax, electron-mediated relaxation thermalizes the nuclei within 10–100 ms [36,48]; this can be prolonged by engineering the electronic relaxation rate [53].

The envelope function $C(\tau_{\text{probe}})$ contains all the information about the nuclear macrostate distribution $p(A_c\Delta I_z)$ via a Fourier transform [54]. Figure 2(d) shows $p(A_c\Delta I_z)$ for the thermal ensemble (red curve), whose full width at half maximum (FWHM) is approximately 313 MHz, in agreement with a standard deviation of $A_c\sqrt{5N/4}$ for $A_c = 0.63(2)$ MHz and $N = 4.9(4) \times 10^4$ (Appendix B 2), and representing a distribution over 497 macrostates FWHM. By comparison, the cooled distribution has a FWHM of 3.6 MHz, equivalent to a probability distribution over approximately 5.7(2) macrostates. We note here that while these macrostates are not necessarily resolved owing to a nonuniform one-to-all hyperfine coupling, the ratio of the width of the distribution to the average A_c is still representative of an effective number of macrostates contained within the distribution.

C. Optimizing feedback in a QD system

We arrive at this global optimal of approximately 6 macrostates by tuning the constitutive variables of the feedback algorithm, namely, the maximal sensing time τ_{max}, the ESR Rabi frequency Ω, and the duration of the actuate gate T. The feedback performance is characterized using two different metrics: the electron dephasing time T_2^*, which we wish to maximize, and an information entropy S_p, which we wish to minimize. The characteristic dephasing time T_2^* is obtained as in Fig. 2 by fitting an envelope $C(\tau_{\text{probe}}) = \exp[-(\tau_{\text{probe}}/T_2^*)^\alpha]$ to the FID data. This T_2^* works well to capture the effect of purifying the spin ensemble as long as the nuclear-spin distribution remains in a single mode, but fails otherwise. The information entropy S_p of $p(A_c\Delta I_z)$ is the limiting density of discrete points (Appendix B 1), where $p(A_c\Delta I_z)$ is the Fourier transform of the FID data. This entropy measure, which extends the notion of Shannon entropy to probability density functions, is a complete, model-independent measure of our data which does not require fitting. It captures the purification in I_z, which we treat as a classical noise source, irrespective of the underlying I degeneracy.

Figure 3(a) shows the electron dephasing time T_2^* (orange circles) and the information entropy S_p (purple triangles) as a function of the maximum sensing time τ_{max}, in a linear sweep from $\tau_{\text{min}} = 30$ ns to τ_{max} [as in Fig. 2(a)]. In Appendix C 1, we verify that this τ_{min} is sufficiently short to ensure a capture range large enough to stabilize the ensemble distribution around a single mode. Our actuate gate has a finite bandwidth (~30 MHz) corresponding to a sensing time of approximately 30 ns, and it is not necessary to use shorter sensing times because nuclear diffusion brings any initial nuclear state to this relatively broad 30 MHz window. We find the optimum τ_{max} at

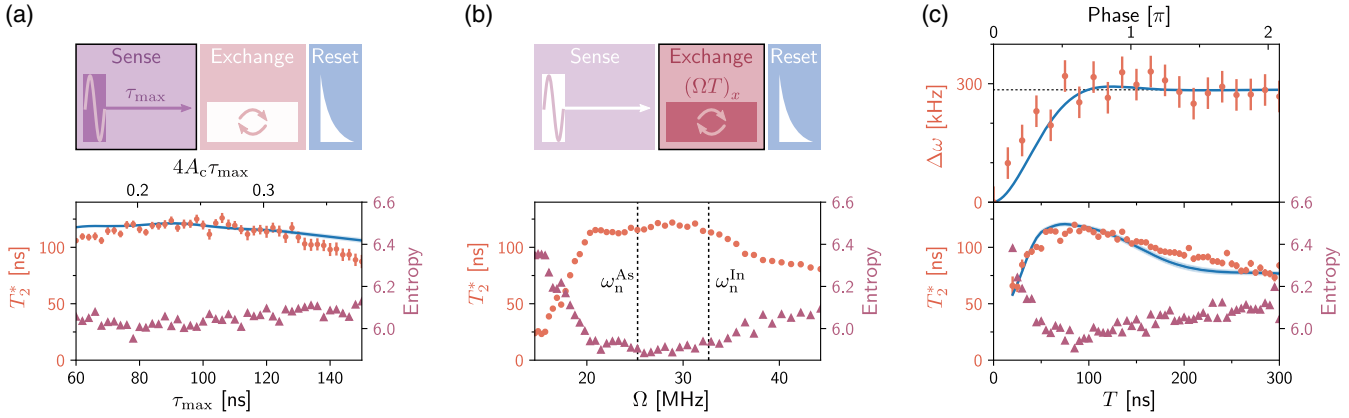

FIG. 3. Optimizing feedback parameters. (a) Top: varying sensing gate τ_{max} in the feedback sequence. Bottom: T_2^* (orange circles, left vertical axis) and entropy S_p (purple triangles, right vertical axis) versus τ_{max} for $\Omega = 29$ MHz and $T = 86$ ns. The blue curve is a fit of T_2^* versus τ_{max} obtained from numerical simulation, with the blue shading as a 68% confidence interval. (b) Top: varying actuate gate Ω and T in the feedback sequence. Bottom: T_2^* (orange circles, left vertical axis) and entropy S_p (purple triangles, right vertical axis) versus Ω for $\tau_{\text{max}} = 100$ ns and $T = 86$ ns. Vertical dashed lines indicate the position of the HH resonances for arsenic and indium. (c) Top: ESR shift from ultraprecise Ramsey measurement [38] as a function of actuate gate duration T (orange circles), fitted (blue curve) with the same microscopic model as for the feedback (Appendix E), shows a maximum population transfer at $T \sim 114$ ns. The fit parameters of this model are $A_c = 0.63(2)$ MHz, $A_{\text{nc}} = 140(13)$ kHz, and a pure nuclear dephasing rate $\Gamma = 6(2)$ MHz. Bottom: T_2^* (orange circles, left vertical axis) and entropy S_p (purple triangles, right vertical axis) versus T for $\Omega = 31$ MHz and $\tau_{\text{max}} = 100$ ns. The blue curve is a fit of T_2^* versus T obtained from numerical simulation, with the blue shading as a 68% confidence interval. The parameters for the simulated T_2^* curves in (a) and (c) are $A_c = 0.63$ MHz, $A_{\text{nc}} = 166(8)$ kHz, and $\Gamma = 6$ MHz.

approximately 90 ns, where the maximum value of T_2^* and the minimum value of S_p coincide. This value is significantly shorter than the theoretical optimum of $1/4A_c \approx 400$ ns given a fitted hyperfine constant $A_c \approx 0.63(2)$ MHz (Appendix E 6). To understand this deviation, we simulate numerically the effect of our cooling algorithm on $N = 49\,000$ spin-1/2 nuclei after mapping the problem to a smaller Hilbert space for computational feasibility. For tractability we further employ exact diagonalization for the unitary evolution during sensing and actuate gates [44], while Kraus operators capture relaxation and dephasing via amplitude- and phase-damping channels (Appendices E 2 and E 3). For independently measured values of $A_c = 0.63$ MHz and pure nuclear dephasing rate $\Gamma = 6$ MHz, we obtain good agreement between simulation (blue curve) and measurements, for $A_{nc} = 166(8)$ kHz and, in line with previous work [37,38], a subset of nuclei (~21 000) partaking in the actuate gate (Appendix E 6).

Our simulations show that electron dephasing during sensing, caused by fluctuations of the finite transverse field $A_{nc}I_x$ [see Eq. (1)], has a strong adverse affect on feedback performance. Furthermore, it explains quantitatively the observed optimal sensing time. We model this process with a semiclassical, transverse magnetic field noise of amplitude $\sim\sqrt{N}A_{nc}$. The highly inhomogeneous noncollinear hyperfine coupling in our QD platform responsible for this noise also reduces the actuate gate fidelity; this can also affect the feedback performance. However, simulations show that even the modest gate fidelity in our system is sufficient to purify down to single-spin fluctuations in the absence of transverse noise (Appendices B 3 and E 7 a). Hence we identify transverse noise during sensing as the main impediment to feedback, which limits the purification of the spin ensemble to approximately 6 macrostates. Importantly, this is not a fundamental feature of the feedback algorithm, or of optically active QDs in general [6,55]. We verify that when this transverse noise is removed the optimum indeed occurs at the expected time $1/4A_c$, and results in purification down to single-spin fluctuations (Appendix E 7).

Figure 3(b) shows the electron dephasing time T_2^* (orange circles) and the information entropy S_p (purple triangles) as a function of the ESR Rabi frequency Ω used to activate the flip-flop exchange gate. With a fixed drive time of $T = 86$ ns we see an optimum Rabi frequency of $\Omega \approx 29$ MHz. This is in close agreement with our theoretical expectation that the strongest feedback occurs when the actuate gate consists of an ESR drive on HH resonance. This QD system exhibits two such resonances at the corresponding Zeeman energies of two nuclear species: arsenic at $\omega_n^{As} = 25$ MHz and indium at $\omega_n^{In} = 33$ MHz. Thanks to the quadrupolar-induced, few-megahertz inhomogeneous broadening of the nuclear Zeeman levels [56], the optimal ESR Rabi frequency occurs around the average of the two resonances.

In seeking to optimize the duration of the activate gate, we expect the optimum setting to leverage the available coherence during the electron-nuclear interaction to achieve a maximal fidelity SWAP gate. As a first step, we thus characterize the coherence of the electron-nuclear interaction in a direct measurement of the electron-nuclear polarization transfer during the exchange gate, as shown in the top panel of Fig. 3(c). Following a preparation sequence as in Fig. 2(a), the probe step alone is replaced with an actuate gate of duration T, which swaps polarization from the electron to a single nuclear magnon, followed directly —without an intervening projective measurement—by an ultraprecise Ramsey measurement [38] that measures the A_c-scale ESR shift induced by the magnon (orange circles). An unconstrained fit of this data with the same modeling approach used for the actuate gate of the algorithm (blue curve) confirms that the electron-nuclear exchange is underdamped, with finite electron-nuclear coherences after the SWAP operation. Maximum population transfer occurs at $T \approx 114$ ns. Furthermore, these data yield a direct measure of the collinear hyperfine constant [38], $A_c = 0.63(2)$ MHz and pure nuclear dephasing rate $\Gamma = 6(2)$ MHz, which we use to constrain the model for the feedback algorithm (Appendix E 6).

Figure 3(c) (bottom panel) shows the electron dephasing time T_2^* (orange circles) and the information entropy S_p (purple triangles) as a function of the duration T of the actuate gate, where we find the optimum at $T \approx 86$ ns. The model values A_{nc} and the number of nuclei partaking in the actuate gate for both the T_2^* dependence and electron-nuclear polarization transfer agree very closely (Appendix E 6). From these values, we would predict an optimum for feedback at the π time of the interaction $T \sim 2/(A_{nc}\sqrt{N/2}) \sim 120$ ns. The approximate agreement between our measured optimum and this simple theoretical estimate confirms that the feedback is optimal close to the maximum achievable fidelity of the SWAP operation. Furthermore, our model informs us that our measured optimum is modified from the theoretical optimum by an optically induced electronic spin relaxation process whose rate is proportional to the power of the incident laser light enabling spin control (Appendix E 3 c) [45]. Under our experimental conditions, this electronic relaxation rate is such that the electron spin is close to completely depolarized when the electron-nuclear exchange reaches its maximum at the π time of the interaction. This can also be seen in the sensing measurement of Fig. 3(c), top panel. When we turn on the actuate gate on an unpolarized electron spin, the effect of the gate is to diffuse the nuclear state away from the lock point. Thus the cooling performance can improve by reducing the drive time T, which in the vicinity of the π time reduces the driven diffusion significantly more than the electron-nuclear polarization transfer. Finally, we verify separately that removing altogether this relaxation process from our numerical simulations indeed returns the

optimal drive time to approximately the π time $\sim 2/(A_{\mathrm{nc}}\sqrt{N/2})$ (Appendix E 7).

D. Tailoring nontrivial spin distributions

Our feedback algorithm allows further engineering of the spin distribution by tuning the feedback curve to host a set of desired locking points—single or multiple. Within the dynamical landscape experienced by the collective spin state I_z, this creates programmable trapping points for the spin ensemble. This is made possible by direct control over parameters that define the sense and actuate quantum gates, namely, the ESR detuning δ, the relative phase ϕ between sense and actuate gates, and the sense time τ.

Using the ESR detuning δ as a tuning parameter, Fig. 4(a) demonstrates precise control over the mean of the I_z distribution by translating the lock point I_z^{lock} from that of an unpolarized ensemble ($I_z^{\mathrm{lock}} = 0$). Our polarizing sequence steps the ESR detuning as a function of time t, $\delta(t) = -A_c I_z^{\mathrm{lock}}$, in steps of 20 MHz, thereby stepping the setpoint by $\sim$30 spin flips, which is detected by the sensing step as a nonzero error signal. At each new value of $\delta(t)$ we perform $\sim$2500 complete cooling sequences to fully correct this error signal. Doing so slowly enough relative to the typical feedback rates and in steps much less than the width of the feedback capture range allows nuclear polarization to build up, leading to an average *dragging* process equivalent to dynamic nuclear polarization [47]. Crucially, we find that the feedback remains stable over a range of fractional nuclear polarization of approximately -20% to $+30\%$, as estimated from the measured Overhauser shift by assuming equal fractional polarization for each species and an indium concentration of 0.5 [56]. This is evidenced by a nuclear-spin distribution whose width remains within a factor of 2 of the optimal and whose information entropy remains largely unchanged over this domain [Fig. 4(a), right-hand panel]. The dynamic locking range, defined as the range of achieved lock points over the width of the distribution, corresponds to well over 1000 distinct accessible macrostates.

Using the relative phase ϕ between the sense and the actuate gates as a tuning parameter, we can transform the probability distribution $p(A_c \Delta I_z)$ from a single-mode to a bimodal distribution, with a programmable frequency-mode splitting equal to the inverse sensing time $1/\tau$. This is done by modifying the first pulse of the algorithm $R_x(\pi/2)$ to have instead a phase ϕ relative to the $R_x(\Omega T)$ actuate gate. This alters the phase of the error signal acquired during sensing, such that $\langle S_x \rangle = -\frac{1}{2}\sin(2\pi A_0 \Delta I_z \tau - \phi)$. Its effect on the feedback curve is shown in Fig. 4(b) (left-hand panel), where given the envelope function associated with our feedback

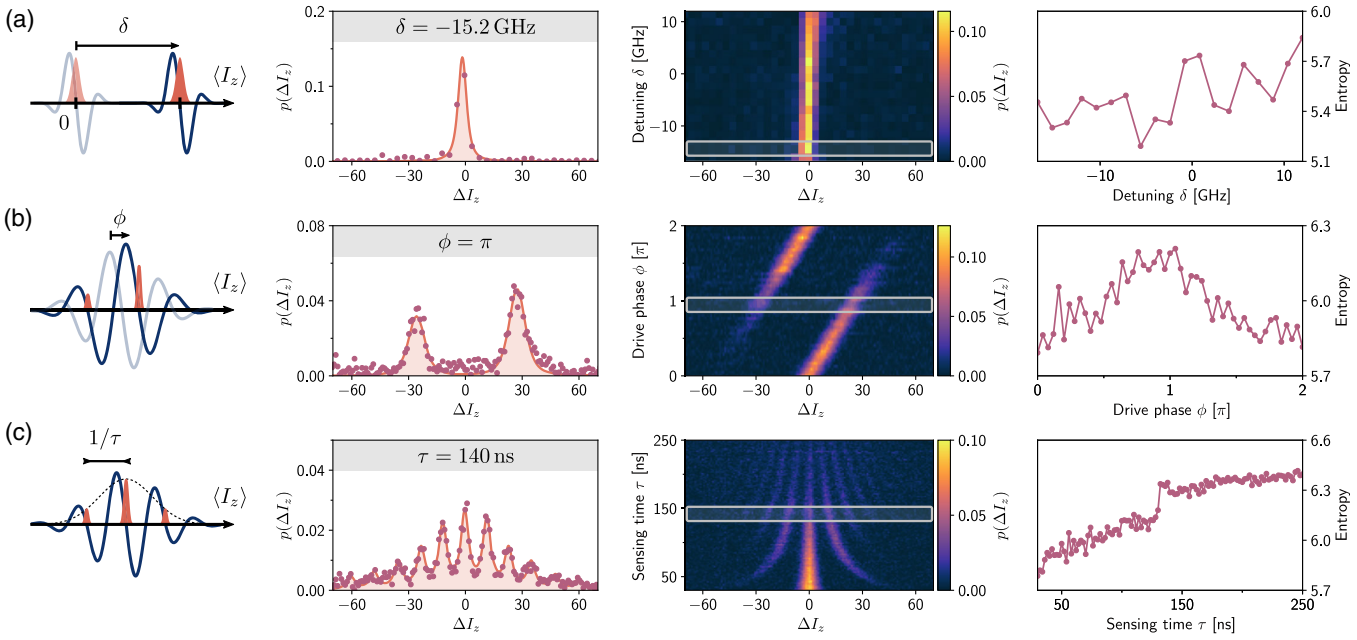

FIG. 4. Engineering spin-ensemble distributions. From left to right: sketch of how the feedback curves (solid blue) are programmed to engineer $p(I_z)$ (orange shaded areas); plots of the measured probability density functions $p(A_c \Delta I_z)$ (purple circles) and their fits (solid curves) at a salient point in the relevant parameter space; full experimental two-dimensional map, from which these salient slices (gray boxes) are taken, showing continuous tuning over the parameter space; information entropy S_p (purple circles) of the $p(A_c \Delta I_z)$ distribution versus the relevant tuning parameter. (a) Varying δ sets the central lock point I_z^{lock} of the feedback. The extrema of the mean field $A_c I_z^{\mathrm{lock}}$ possible with our feedback algorithm are $+12.0$ GHz and -15.2 GHz, where the FWHM of $p(A_c \Delta I_z)$ are measured as 5.9 and 3.7 MHz, respectively. (b) Tuning the drive phase ϕ allows continuous variation between mono- and bimodal feedback as seen in the $\phi - \Delta I_z$ map. (c) Using a single sensing time τ during feedback determines a well-defined steady-state lock point splitting. Varying τ in the two-dimensional map shows we can tune the number of modes in the probability distribution.

bandwidth, the phase ϕ is equivalent to a carrier-envelope phase. By changing this phase, we can tune the relative weight of the two possible modes of the distribution, as shown in the two-dimensional map of Fig. 4(b), for values of ϕ from 0 to 2π. As can be seen from the right-hand panel of Fig. 4(b), the entropy is maximized for $\phi = \pi$, where there exists an equal weighting between the two modes. This particular point can be seen as a balanced classical mixture of two I_z states separated by ∼55 nuclear spin flips, each with a width of a few spins. Detecting this classical signal is a first step toward the investigation of a Schrödinger kitten state [57]: in this case a quantum superposition of two collective states with small nuclear polarization.

Finally, using the sense time τ as a tuning parameter, we create multimodal frequency-comb-like spin distributions. To do so, we apply a fixed sense time τ during our feedback sequence [Fig. 2(a)], which tunes a correspondingly fixed capture range, set by the spacing $1/A_0\tau$ between two lock points within the feedback function. When this capture range is smaller than the width of the initial nuclear distribution, the nuclear state I_z probabilistically falls into any one of the lock points contained within the initial distribution, as shown in Fig. 4(c) (left-hand panel). In Fig. 4(c), we demonstrate this for $\tau = 40$ ns to $\tau = 250$ ns, achieving from 3 to 11 simultaneous modes of the spin distribution, respectively. Strikingly, at the long sensing times $\tau \gtrsim 140$ ns, the initial state is frozen into $\gtrsim 9$ modes, each with a width of 3.3 MHz or approximately $5A_c$, which is narrower than the 3.6 MHz width measured for the optimal single-mode preparation. The increased feedback strength at these long sensing times gets the system closer to its ultimate narrowing limit at the expense of populating other nearby modes. While the individual modes of the distribution become narrower, the information entropy [Fig. 4(c), right-hand panel] of the overall distribution increases with sensing time as the distribution is spread over an increasingly large phase space. These multimode spin distributions can be seen as a freezing of the initial state onto a one-dimensional lattice of points in the phase space of nuclear polarization, which we call latticed multistability. Because of a finite probability of hopping between lattice sites, integrating over a sufficiently long time yields the observed ensemble average. With added phase coherence between sites, this lattice could simulate a one-dimensional quantum walk where the lattice spacing and depth can be tuned with the sensing time and the amplitude of electronic coherence during sensing, respectively.

III. TOWARD SCHRÖDINGER KITTEN STATES OF THE NUCLEAR ENSEMBLE

We have thus far demonstrated control over the modes of a spin distribution via a tailored dynamical landscape that is equivalent to engineering classical mixtures of collective states on demand. However, the actuation gate fundamentally generates quantum coherences between the electron and the collective nuclear state, which have thus far been eliminated during electronic reset. As such, we propose an extension to the algorithm to include a disentangling step, which maps electron-nuclear coherences to purely nuclear ones, prior to electronic reset. This preserves nuclear coherences and allows the engineering of quantum states of the ensemble. Figure 5 depicts a concrete example of an extension designed to engineer Schrödinger kitten states [57], which we discuss in more detail in Appendix E 8. In short, the disentangling operation is performed by a free evolution, which is present in the original algorithm between the actuation and reset steps. If the evolution time is chosen appropriately, the free evolution performs an electronic rotation conditional on the nuclear state, producing a separable electron-nuclear state. Starting from a purified nuclear state, which is precisely what our feedback algorithm is designed to prepare, the operation of our minimally modified algorithm can generate quantum superpositions $|\psi\rangle = |I, I_z + M\rangle + e^{i\phi_M}|I, I_z - M\rangle$. Note that to achieve $M > 1$, one needs to further modify the algorithm to repeat actuation M times, as in Fig. 5. The state $|I, I_z + M\rangle$ is a collective state of the entire ensemble, and such a quantum superposition is thus analogous to a Schrödinger kitten state. In our InGaAs QD platform the low fidelity of the actuation gate, owing to considerable nuclear inhomogeneity, prevents an experimental realization of this modified algorithm. However, recent work on

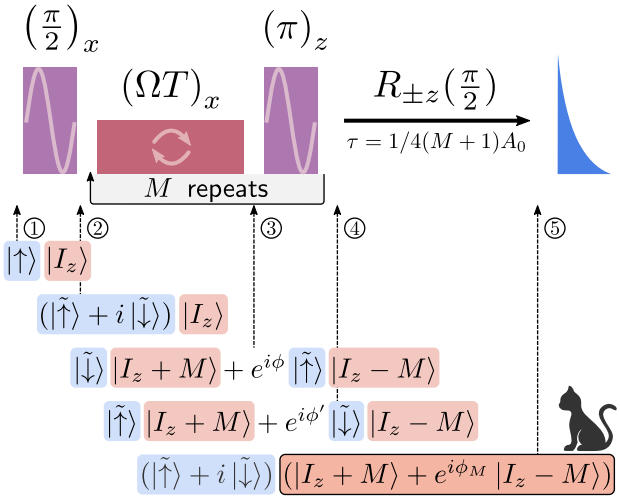

FIG. 5. Preparation of a Schrödinger kitten state. The quantum state preparation sequence closely resembles that of the elementary unit of our feedback algorithm [Fig. 2(a)], but with two modifications. Firstly, a $(\pi)_z$ rotation of the electron after the actuate gate allows us to repeat actuation M times for the excitation of M magnons. Secondly, the wait time between actuation and reset is now precisely chosen to perform a $(\pi/2)$ rotation about the z axis conditional on the nuclear state, $R_{\pm z}(\pi/2)$. Markers 1–5 track the quantum state evolution during the preparation sequence. The relative phase ϕ comes from evolution under the nuclear Zeeman and hyperfine terms and, while precisely known, is inconsequential.

lattice-matched GaAs QDs has shown greatly reduced nuclear inhomogeneities [6,55], promising a realization of our extended quantum algorithm in the near future.

IV. DISCUSSION

We presented a quantum-algorithmic approach to feedback to stabilize the fluctuations of an ensemble down to single quanta. It can be applied to a central spin or central boson that can do the following: sense the collective state of an ensemble via an Ising coupling; modify the collective state of the ensemble via an exchange coupling (e.g., a hyperfine interaction combined with single or double resonance at the HH condition); and be reinitialized with little backaction on the ensemble. This means that our algorithm can be applied to a wide range of physical platforms including quantum dots in III-V materials (InGaAs, GaAs), rare-earth ions, donor spins in silicon, and defect centers in diamond and SiC [58].

Despite the substantial noise and inhomogeneity inherent in our QD nuclear-spin ensemble, applying our feedback algorithm to this system enabled an 83-fold reduction in spin fluctuations, purifying to within a factor 3 of the single-quantum limit. Compared to the previous state of the art, where a 20-fold reduction was reported [37], our feedback approach further reduces spin fluctuations by a factor 4. Incidentally, we also report here the longest inhomogeneous dephasing time to date for any spin qubit in optically active quantum dots: $T_2^* = 296(5)$ ns for a second QD investigated in less detail but with fully consistent feedback performance (Appendix C 3). Yet we stress that the primary achievement of this work is the conceptual leap from a continuous, driven, dissipative feedback approach to an algorithmic one, capable of suppressing and engineering spin noise down to single-spin fluctuations.

Indeed, we demonstrated the engineering of nontrivial classically correlated nuclear states, including a classical mixture of two I_z states separated by tens of spin flips: a classical precursor to a Schrödinger kitten state of nuclei. To this end we formulated a concrete proposal for the extension of this algorithm for the production of quantum superpositions of collective states. A future direction also includes investigating the limit cycle during feedback operation at the single-spin level: applying the algorithm to an initial pure state $|I_z\rangle$, the nuclear state would cycle between $|I_z\rangle\langle I_z| \leftrightarrow \frac{1}{2}(|I_z-1\rangle\langle I_z-1| + |I_z+1\rangle\langle I_z+1|)$ subharmonically with a periodicity twice that of the algorithm. The appearance of this limit cycle could be a witness for the dissipative preparation of a well-defined total angular momentum state [48] I constituting the initialization of a pure Dicke state in this central-spin system.

ACKNOWLEDGMENTS

We acknowledge support from the U.S. Office of Naval Research Global (N62909-19-1-2115), ERC PHOENICS (617985), EPSRC NQIT (EP/M013243/1), EU H2020 FET-Open project QLUSTER (862035), and EU H2020 Research and Innovation Programme under the Marie Skłodowska-Curie grant QUDOT-TECH (861097). Samples were grown in the EPSRC National Epitaxy Facility. D. A. G. acknowledges support from a St John's College Fellowship and a Royal Society University Research Fellowship, and C. L. G. acknowledges support from a Dorothy Hodgkin Royal Society Fellowship.

The authors declare that they have no competing interests.

D. A. G., C. L. G., and M. A. conceived and supervised the experiments. D. M. J. and U. H. implemented and carried out the experiments. D. M. J. and U. H. performed the data analysis. L. Z. and D. M. J. developed the theory and performed the simulations, with guidance from C. L. G. and D. A. G. E. C. and M. H. grew the material. All authors contributed to the discussion of the analysis and the results. All authors participated in preparing the manuscript.

APPENDIX A: EXPERIMENTAL METHODS

1. Setup

a. Sample

The heterostructure of the wafer used in this work, which has been used in previous studies [36,45,48,56,59], is depicted schematically in Fig. 6. The InGaAs QD layer (shown in red) is capped above and below with GaAs (gray). The layer below is 35 nm deep and forms a tunnel

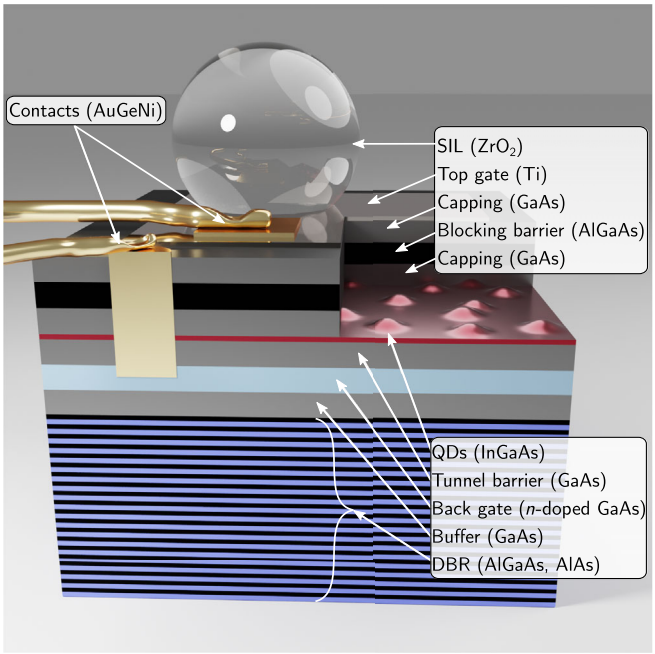

FIG. 6. Sample. A 3D render of the heterostructure of our QD sample (not to scale) with a cutout above the QD layer. A full breakdown of the structure is given in the text. Abbreviations: DBR, distributed Bragg reflector; SIL, solid immersion lens.

barrier between the QD and the Fermi sea of the *n*-doped GaAs back contact (light blue). The back contact combined with the semitransparent titanium top gate (6 nm) forms a Schottky diode structure which allows us to control the charge state of the QD. An electron in the ground state is a stable configuration for a time $T_1 = 50\ \mu$s thanks to a tunnel barrier between the QD layer and the Fermi sea of the back contact. The two diode gates are electrically contacted with Ohmic AuGeNi contacts (shown in gold). Above the top capping layer is a blocking barrier of AlGaAs (black) to prevent charge leakage, and then a final capping of GaAs. At the bottom of the heterostructure is a distributed Bragg reflector to improve photon emission from the top surface. The photon collection is further enhanced to 10% at the first lens with a superhemispherical cubic-zirconia solid immersion lens.

b. Optics

Figure 7 shows the optical and microwave setup. We use a confocal microscope with crossed polarizers on excitation and collection arms to excite the QD resonantly, and collect its emission. We excite the QD with circularly polarized light by using a quarter wave plate between the polarizers. The collected emission is spectrally filtered with an optical grating with a 20 GHz passband before being sent to a superconducting-nanowire single-photon detector (SNSPD, Quantum Opus One).

Two lasers are required for our experiments. The first—a New Focus Velocity laser diode—is resonant with the $|{\downarrow}\rangle \leftrightarrow |{\Downarrow}\uparrow{\downarrow}\rangle$ transition and is used for spin pumping and electron spin readout (reset). The second is used for electron-spin control via a two-photon stimulated Raman process [45] and is generated by a Toptica DL Pro laser diode fed through a Toptica BoosTA tapered amplifier. This Raman laser is 800 GHz detuned from the trion excited state manifold. As required for Raman control, we derive two coherent laser fields from this single mode by feeding it through a fiber-based EOSPACE electro-optic amplitude modulator (EOM), which is driven with a microwave waveform (Appendix A 1 c). The resulting first-order sidebands after amplitude modulation are two coherent laser fields, separated by twice the microwave drive frequency $\omega_{\mu w}$, and whose relative phase is twice the phase of the microwave [45]. With these we can drive the electron-spin resonance at a frequency $\omega = 2\omega_{\mu w}$.

c. Microwave

Controlling the electron spin with a two-photon Raman process gives us effective microwave control over its Bloch vector. We can control the Rabi frequency, phase, and detuning of the qubit drive by modifying, respectively, the power, phase, and frequency of the EOM's microwave drive, all of which are imprinted onto the Raman beams by the EOM. An experimental sequence is thus defined by a microwave signal where all of these parameters, along with

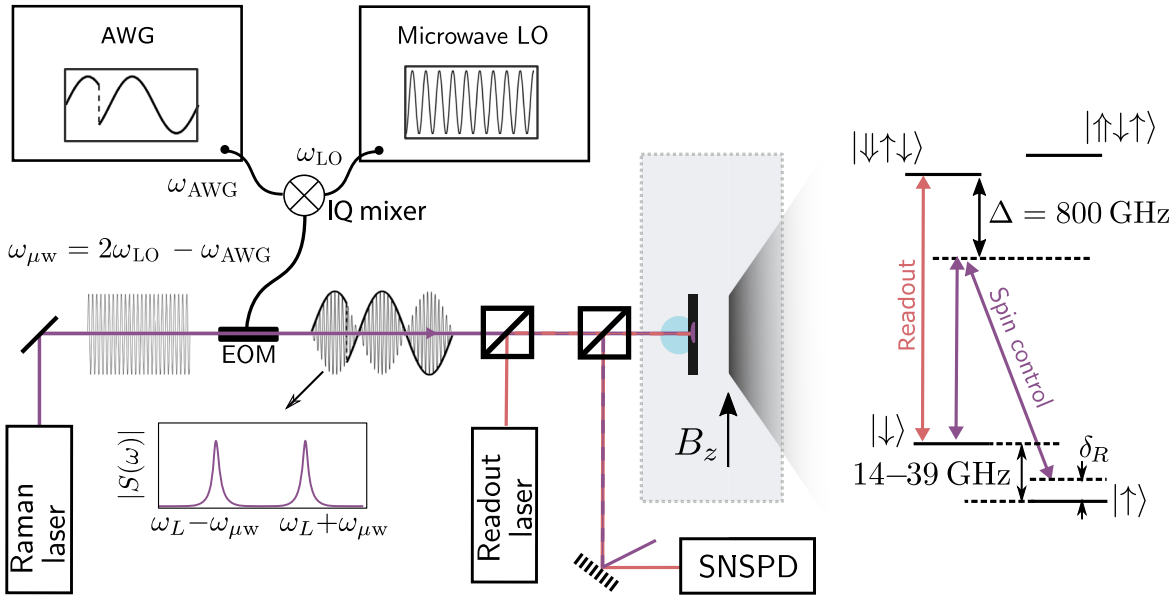

FIG. 7. Optical and microwave setup. Adapted from Ref. [48]. From left to right we have a Raman laser 800 GHz detuned from the trion manifold that is fed through an electro-optic modulator (EOM). The EOM is driven by a microwave signal derived from the IQ mixing of an arbitrary waveform generator (AWG) with a local oscillator (LO). The EOM output is then 2 coherent laser fields. A beam splitter combines the Raman laser with a resonant laser for readout, which is sent to the sample. The sample sits in a bath cryostat at 4 K, with a 3.5 T magnetic field applied in Voigt geometry. The QD emission is collected and excitation light is filtered by polarization and color before being counted on a superconducting-nanowire single-photon detector (SNSPD). The rightmost section depicts the QD energy level diagram and excitation laser frequencies.

pulse timing and duration, are set programmatically with an arbitrary waveform generator (Tektronix AWG70001A), at a sampling rate of 6 Gsamples/s. We use 2 channels of the AWG to produce the I and Q components of this signal, which has a carrier frequency of $\omega_{\mathrm{AWG}} = 600$ MHz. With these we can perform single-sideband mixing with a frequency-doubled local oscillator (LO) of frequency $\omega_{\mathrm{LO}} \in [3.665, 10.065]$ GHz to up-convert to the final microwave frequency $\omega_{\mu\mathrm{w}} = 2\omega_{\mathrm{LO}} - \omega_{\mathrm{AWG}}$. The IQ mixer, which is an Analog Devices ADRF6780 board, handles internally the frequency doubling of the LO, which is derived from a Rohde & Schwarz SMF100A source.

2. Techniques

a. Full experimental pulse sequence

Figure 8 depicts the pulse sequence that makes up a single repeating block of the experiment. This block repeats at a rate of 50 kHz and is composed of a 15 μs pump section, where we run the feedback algorithm to prepare a target state of the nuclear ensemble, and a 5 μs probe section, where we measure the resulting electronic free-induction decay to extract the probability distribution $p(A_c \Delta I_z)$. The pump section is described in detail in the main text. The probe section consists of four separate Ramsey interferometry measurements, two of which probe the spin-$\uparrow$ population, $\rho^e_{\uparrow\uparrow}$, and two of which probe $\rho^e_{\downarrow\downarrow}$. Having two of each is not necessary, and is only done to improve the signal-to-noise ratio.

Selecting which spin population we read out is done as follows: The readout laser is always resonant with the $|\downarrow\rangle \leftrightarrow |\Downarrow \uparrow \downarrow\rangle$ transition making $|\downarrow\rangle$ the bright state. Thus we select which population to read out by choosing to swap the electron spin populations with a π pulse before optical pumping, yielding a spin fluorescence signal, $S_{\downarrow\downarrow}$ or $S_{\uparrow\uparrow}$, proportional to the population, $\rho^e_{\downarrow\downarrow}$ or $\rho^e_{\uparrow\uparrow}$, respectively. In practice we replace this additional π pulse with a π phase on the second Ramsey gate, which achieves the same result. This avoids an erroneous disparity in the two populations that would result from the addition of a pulse with finite fidelity. Note that S is the integrated fluorescence over the entire spin-pumping transient after background subtraction. We may then calculate the average spin populations:

$$\rho^e_{\uparrow\uparrow} = \left\langle \frac{S^1_{\uparrow\uparrow} + S^2_{\uparrow\uparrow}}{S^1_{\uparrow\uparrow} + S^2_{\uparrow\uparrow} + S^1_{\downarrow\downarrow} + S^2_{\downarrow\downarrow}} \right\rangle, \tag{A1}$$

where we combine the two repeated spin readouts, 1 and 2, for improved signal-to-noise ratio, and we average over the many repetitions made during a given integration time. Finally, we note that each of the 4 Ramsey interferometry measurements has a phase $\theta = 2\pi\tau_{\mathrm{probe}}\omega_{\mathrm{serr}}$ added to the second $(\pi/2)$ gate, where ω_{serr} is a serrodyne frequency. This adds a Fourier component at frequency ω_{serr} to the FID making fitting the decay envelope robust against a few-megahertz systematic detuning arising from the optical Stark shift during the Ramsey gates [38].

b. Polarization protocol

In the main text we describe how we can polarize the QD nuclear ensemble by stepping in time the ESR drive detuning, $\delta(t) = \omega_e - \omega = -A_c I_z^{\mathrm{lock}}$. We achieve this by varying the LO frequency in discrete steps $\Delta\omega_{\mathrm{LO}}$ resulting in steps of detuning $\Delta\delta = -4\Delta\omega_{\mathrm{LO}}$. In this way we step the detuning by 20 MHz every ~50 ms, amounting to ~2500 repeats of the entire experimental sequence (Appendix A 2 a) per step ensuring that the nuclear-spin system reaches steady state at every step. As we polarize the nuclei, the resulting Overhauser shift alters the electron-spin splitting and thus the optical transition frequency to the trion manifold. In order to polarize beyond the trion linewidth we therefore need to compensate this effect with a dc Stark shift. We step the Schottky diode gate bias with the LO frequency to maintain single-photon resonance with the fixed-frequency readout laser.

APPENDIX B: ADDITIONAL NOTES ON DATA ANALYSIS

1. Entropy

In the main text, the concept of entropy was applied to quantify the purity of an arbitrary distribution. To this end, we employed the limiting density of discrete points, which is an extension of Shannon entropy to continuous probability distributions. It is defined by

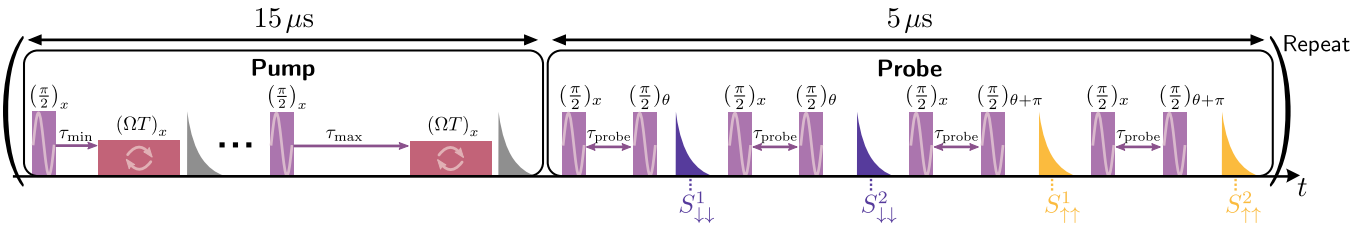

FIG. 8. Experimental pulse sequence. A schematic of the ESR control pulses (pink and red square pulses) and readouts (gray, purple, and yellow spin-pumping transients) that make up a single repeating block of the entire experiment (timings not to scale). The purple and yellow spin-pumping transients correspond to reading out opposite electronic spin populations, achieved with a relative π phase shift on the second Ramsey gate $(\pi/2)_{\theta+\pi}$. The phase of the second Ramsey gate is serrodyned at a frequency ω_{serr} via $\theta = 2\pi\tau_{\mathrm{probe}}\omega_{\mathrm{serr}}$.

$$H_N(X) = \log(N) + H(X),$$
$$\text{with} \quad H(X) = -\int p(x) \log \frac{p(x)}{m(x)} dx,$$

where N is the number of points discretizing the continuous distribution $p(x)$, and $m(x)$ is an invariant measure of the density of points as $N \to \infty$.

In our case, we evaluated the probability distribution $p(A_c \Delta I_z)$ in the range from −250 to 250 MHz; hence, $m(x) = 2\ \text{GHz}^{-1}$. We chose $N = 800$, which leads to a constant offset of $\log 800 \approx 6.7$.

2. Calculating number of nuclei

We can extract the number of nuclei in the QD from a measurement of the hyperfine constant per nucleus A_c and T_2^* at thermal equilibrium at infinite temperature. The former is provided by the ESR-shift measurement [38] reported in Fig. 3(c) of the main text, and the latter from the FID in Fig. 2(c) of the main text. This FID was measured at thermal equilibrium at 4 K, which is effectively infinite temperature when comparing to the relevant nuclear Zeeman energy scale. This means we can safely assume that the nuclear state is fully mixed. In this case the nuclear probability distribution is a Gaussian, $p(\Delta I_z) = e^{-\Delta I_z^2/2\sigma^2}$, with standard deviation given by

$$\sigma^2 = \langle I_z^2 \rangle = \left\langle \left(\sum_i^N I_{i,z} \right)^2 \right\rangle = \sum_i^N \langle I_{i,z}^2 \rangle = \frac{1}{3} N I_j (I_j + 1),$$

where i indexes an individual spin and we have assumed $\langle I_z \rangle = 0$. Taking a single species with $I_j = 3/2$ gives $\sigma = \sqrt{5N/4}$. Since $p(\Delta I_z)$ and the FID are related by a Fourier transform, the FID is also Gaussian with $T_2^* = 1/\sqrt{2}\pi A_c \sigma$. Using $T_2^* = 1.52(5)$ ns and $A_c = 0.63(2)$ MHz we can then calculate $N = 49(4) \times 10^3$.

One can also extract an estimate of N from T_2^* by using the hyperfine constants of the material and assuming an indium concentration [56]. Since indium is the species with the highest spin and the largest hyperfine constant, its concentration has a significant effect on N, which can range from 48 000 to 110 000 for concentrations from 0.2 to 0.7. As such, our estimate of $N = 49\,000$ is entirely reasonable.

3. Quantum gate fidelities

We seek to give some quantification of gate fidelities using the following simple metric [45]: we calculate a quality factor Q for the electronic and electron-nuclei Rabi oscillations separately, which is the ratio of the $1/e$ time to the π time of the oscillations. From this we calculate a fidelity $F = (1 + e^{-1/Q})/2$. For the electronic Rabi oscillations (not shown) we calculate $Q = 34$, yielding $F = 98.6\%$. For the electron-nuclear exchange [Fig. 3(c), top panel], we separately fit an unconstrained, damped simple harmonic oscillator model to the data [38], resulting in $Q = 1.65$, yielding $F = 77\%$.

APPENDIX C: ADDITIONAL DATA

1. Minimum feedback capture range

As detailed in the main text, if we seek to purify the nuclear ensemble to a single mode we must start feedback with a sufficiently broad capture range as not to populate the next-nearest stable points, Fig. 1(c). Given the feedback bandwidth of ∼30 MHz, determined by the width of the HH resonance, we expect that the broadest capture range we require is $1/\tau_{\min} \sim 30$ MHz or equivalently $\tau_{\min} \sim 33$ ns. In this way, at the beginning of the feedback preparation sequence the next-nearest stable points are beyond the bandwidth of the feedback and thus are very weak attractors ensuring purification to a single mode. In Fig. 9 we plot the results of an identical experiment to Fig. 3(c) of the main text, i.e., feedback with a single sensing time, but for small τ. From this we can see a region of $\tau \lesssim 35$ ns where it is not possible to populate neighboring stable points which justifies using $\tau_{\min} = 30$ ns throughout our experiments.

2. Hahn echo

We note here that our quantum-algorithmic purification has no appreciable effect on the electron-spin coherence time as measured in Hahn echo. Figure 10 reports a Hahn-echo measurement after optimal purification of the nuclear spin bath (purple circles) and an accompanying exponential fit (yellow curve). The extracted $T_2^{\text{HE}} = 1.10(9)$ μs is a typical value for QDs on this wafer for a nuclear ensemble at thermal equilibrium at 4 K and magnetic field of 3.5 T [37,56].

3. Second quantum dot

By way of gathering statistics we tested our algorithmic cooling on a second quantum dot, QD2. After the same optimization procedures performed on QD1 of the main

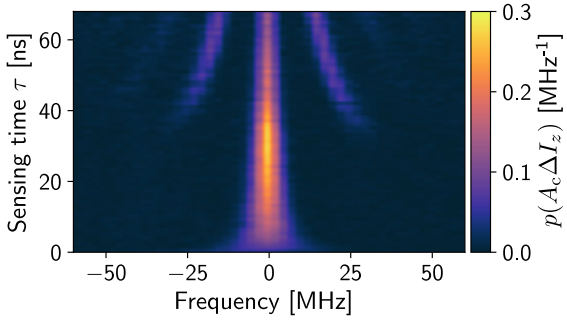

FIG. 9. Minimum capture range. 2D plot of $p(A_c \Delta I_z)$ versus frequency, $A_c \Delta I_z$, and sensing time τ. In this experiment we do not dynamically sweep the sensing time, but rather use a constant value for all 44 repeats (per preparation cycle) of the algorithm. For sufficiently small $\tau \lesssim 35$ ns we avoid multistability and prepare a single-mode distribution.

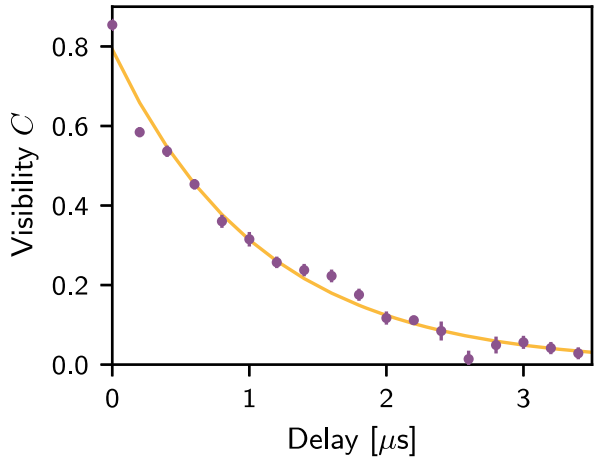

FIG. 10. Hahn echo after optimal purification. Hahn-echo visibility versus delay (purple circles) is fitted with an exponential decay (yellow curve) to extract a $T_2^{\mathrm{HE}} = 1.10(9)$ μs.

text, we plot in Fig. 11 the FIDs for QD2 at thermal equilibrium (triangles) and after purification (circles). From these data, and using the same notation as the main text, we extract fit parameters of $T_2^* = 3.3(3)$ ns, $\alpha = 1.9(4)$ and $T_2^* = 296(5)$ ns, $\alpha = 1.65(8)$ for thermal and purified, respectively. Although the purified T_2^* is 2.4 times longer than QD1, the improvement factor from thermal equilibrium is 89, entirely consistent with QD1. Compared to the previous state-of-the art feedback approach [37] (purple curve), our algorithmic feedback reduces spin fluctuations by a further factor 5. We do not plot the corresponding

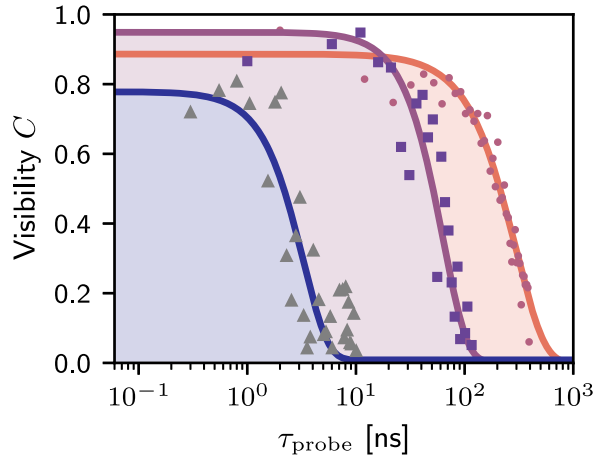

FIG. 11. FIDs for QD2. Triangles, squares, and circles are the FID envelopes resulting from a nuclear-spin ensemble at thermal equilibrium, after state-of-the art purification [37], and after our optimal purification, respectively. Fitting these data with the blue, purple, and orange $C(\tau_{\mathrm{probe}})$ curves yields $T_2^* = 3.3(3)$ ns, $\alpha = 1.9(4)$; $T_2^* = 64(3)$ ns, $\alpha = 2.0(2)$; and $T_2^* = 296(5)$ ns, $\alpha = 1.65(8)$, respectively.

curve for QD1, but we note here that the improvement over the state of the art is similar: a factor 3.

Despite the optimally purified T_2^* being 2.4 times longer for QD2 than QD1, it represents worse purification in terms of an absolute number of nuclear macrostates: Comparing the T_2^* values of the two QDs at thermal equilibrium tells us that QD2 contains approximately 4.7 times more nuclei, and its hyperfine constant per nucleus A_c is 4.7 times smaller [56]. Thus, although the width of $p(A_c \Delta I_z)$ for QD2 is 2.4 times narrower in frequency space ($A_c \Delta I_z$), its width in absolute macrostates (ΔI_z) is 2.0 times larger than QD1, and is less pure.

APPENDIX D: FEEDBACK FUNCTION FORMALISM

With the spin bath evolving under drive and dissipation we can construct semiclassically a rate equation that captures the evolution of the mean value $\langle I_z \rangle$ valid over a coarse-grained timescale much larger than the time of a single algorithm cycle [40,47]. We stress that the fully quantum approach used in our modeling (Appendix E) is the most complete, but we can nevertheless gain intuition about the feedback with this method. The algorithm itself results in directional $\langle I_z \rangle$-changing rates $W_{\pm}(\langle \Delta I_z \rangle)$ that stabilize the value of $\langle I_z \rangle$. Further, there will be relaxation processes in any central-spin system that lead to spin diffusion, either intrinsic or electron mediated, which rethermalizes the bath at a rate Γ_d. For example, in our QD system electron-mediated nuclear-nuclear spin interactions [60,61] lead to diffusion at a rate $\mathcal{O}(10\ \mathrm{Hz})$ [48]. The rate equation then reads

$$\frac{d\langle I_z \rangle}{dt} = W_+(\langle \Delta I_z \rangle) - W_-(\langle \Delta I_z \rangle) - \Gamma_d \langle I_z \rangle. \tag{D1}$$

The directional rates can be constructed intuitively, since we will drive one spin flip per algorithm cycle in response to a ΔI_z fluctuation provided $\tau = 1/4A_0 \Delta I_z$. Assuming unitarity in the flip-flop interaction and that one cycle takes $\tau + 1/2A_{\mathrm{ff}}$, neglecting the spin-pumping time, we have

$$W_{\pm}(\langle \Delta I_z \rangle) = \frac{1 \mp \sin[2\pi A_0 \langle \Delta I_z \rangle \tau]}{2\tau + 1/A_{\mathrm{ff}}}. \tag{D2}$$

The feedback curve then becomes

$$\frac{d\langle I_z \rangle}{dt} = \frac{-\sin[2\pi A_0 \langle \Delta I_z \rangle \tau]}{\tau + 1/2A_{\mathrm{ff}}} - \Gamma_d \langle I_z \rangle, \tag{D3}$$

which we report in the main text with $\Gamma_d \ll 1/\tau + 1/2A_{\mathrm{ff}}$.

APPENDIX E: MODELING

1. Outline

We seek to model the coupled electron-nuclear dynamics in our QD system during the feedback algorithm. From the resulting complete density matrix we may take a partial trace over the electron to leave only the density matrix of the nuclear-spin system. From this we calculate $p(I_z)$ and compare to our experimental data via either of our feedback metrics: entropy or T_2^*.

The nuclear ensemble comprises three species: arsenic ($I = 3/2$), indium ($I = 9/2$), and gallium ($I = 3/2$), but we may safely neglect gallium's contribution to the feedback dynamics owing to a much weaker quadrupolar contribution [56]. To reduce the computational complexity of our model we make our first approximation: we run two independent simulations for arsenic and indium separately and average the results. In this way we avoid squaring the dimensionality of the nuclear Hilbert space and its associated complexity.

Our second simplifying approximation is to model the nuclei as an ensemble of N spin-1/2 particles, with a uniform hyperfine coupling to the electron. This allows us to parametrize the nuclear state by the set of quantum numbers I, I_z, where the integers I and I_z range from 0 to $N/2$ and $-I$ to I, respectively. In this way we reduce the calculation on the full (2×2^N)-dimensional Hilbert space to $N/2$ calculations on $2 \times (2I+1)$-dimensional Hilbert spaces, which are uncorrelated and evolve independently. In this basis the full electron-nuclear density operator can be written as

$$\rho = \sum_{S_z} \sum_{S_z'} \sum_{I,I_z} \sum_{I',I_z'} \rho_{S_z,S_z',I,I_z,I',I_z'} |S_z\rangle\langle S_z'| \otimes |I, I_z\rangle\langle I', I_z'|. \tag{E1}$$

Solving for the driven-dissipative dynamics of the coupled electron-nuclear system via a Lindblad master equation requires the use of superoperators of size $D^2 \times D^2$, where D is the Hilbert space dimensionality. In each I manifold we have $D = 2(2I+1)$, meaning that for realistic $N \sim 10^5$, the large-I manifolds would require prohibitively large matrices of size $N^2 \times N^2$ to represent the superoperators. To overcome this we make a second approximation to split the evolution into distinct unitary quantum operations and nonunitary dissipation and dephasing operations. This reduces the computational complexity to simple $D \times D$ matrix multiplication for both coherent processes, via exact diagonalization, and incoherent processes, via Kraus operators.

Even after reducing the matrix size to $D \times D$, this is still prohibitively large for manifolds of $I \sim N \approx 10^5$, which is where the third approximation comes in: manifolds of very large I can be neglected. This is because we weight the outcome of a simulation in a given I manifold ρ_I by its degeneracy when calculating the final expectation value of any observable A:

$$\mathrm{Tr}\rho A = \sum_I w_{I,N} \mathrm{Tr}\rho_I A. \tag{E2}$$

We calculate these weights exactly in Appendix E 5, but suffice to say that they are peaked strongly around $I = \sqrt{N/2} \approx 160$, and decay exponentially with I from there on. As such, assuming I is indeed distributed thermally according to these weights, we capture the vast majority of the dynamics by a coarse-grained simulation in only 46 manifolds with I values of $0, 14, 28, \ldots, 630$. In each of the manifolds we further truncate the Hilbert space by only simulating with I_z values ranging from $-I/14$ to $I/14$, i.e., only around states of low polarization, which is a good approximation given that our feedback procedure purifies the nuclear state very close to the zero-polarization macrostate.

2. Unitary evolution during the algorithm

During the sensing and actuate parts of step j of the feedback algorithm we consider the unitary part of the evolution to act on the density operator in the usual way:

$$\rho_{j+1} = U_j \rho_j U_j^\dagger. \tag{E3}$$

The engineered Hamiltonians during sensing and actuation are $H_{\mathrm{sense}} = \delta S_z + \omega_n I_z + A_{\mathrm{c}} S_z I_z + A_{\mathrm{nc}} S_z I_x$ and $H_{\mathrm{act}} = \Omega S_x + \omega_n I_z - (A_{\mathrm{nc}}/4)(\tilde{S}_+ I_- + \tilde{S}_- I_+)$, respectively, where $\tilde{S}_\pm = S_z \pm i S_y$. Given these, the unitary evolution during step j of the algorithm is generated by

$$U_j = \underbrace{e^{-iTH_{\mathrm{act}}}}_{U_{\mathrm{act}}} \underbrace{e^{-i\tau_j H_{\mathrm{sense}}}}_{U_{\mathrm{sense,j}}} \underbrace{\frac{1}{\sqrt{2}}(\mathbb{1} - i\sigma_x)}_{R_x(\frac{\pi}{2})}, \tag{E4}$$

where $R_i(\theta)$ represent rotations of angle θ about axis $i = x$, y, z, and σ_i are the Pauli matrices.

The action of $U_{\mathrm{sense,j}} R_x(\pi/2)$ on the density operator expressed as in Eq. (E1) is straightforward, provided we assume $A_{\mathrm{nc}} \ll A_{\mathrm{c}}$ and neglect the $A_{\mathrm{nc}} S_z I_x$ term—we reintroduce the effect of $A_{\mathrm{nc}} S_z I_x$ with a semiclassical approximation in Appendix E 3. In this case H_{sense} is diagonal in the $|S_z\rangle \otimes |I, I_z\rangle$ basis and the matrix exponential of $U_{\mathrm{sense}} R_x(\pi/2)$ leads to a simple phase acquisition. The action of U_{act} is less straightforward to compute since H_{act} is not diagonal. We first rewrite as $U_{\mathrm{act}} = e^{-iTH'_{\mathrm{act}}} R_{-y}(\pi/2)$, where $H'_{\mathrm{act}} = \Omega S_z + \omega_n I_z - (A_{\mathrm{nc}}/4)(S_+ I_- + S_- I_+)$, which is 2×2 block

diagonal and can be diagonalized efficiently [44]. The price we pay for this computational speedup is the implicit assumption that the electron-nuclear actuate gate is performed exclusively on HH resonance [50,51], otherwise block diagonality is broken. To this end we model two nuclear species by running two simulations with nuclear Zeeman frequencies $\omega_n^{\mathrm{As}} = 25.3$ MHz and $\omega_n^{\mathrm{In}} = 32.7$ MHz, in each case imposing HH resonance, and average the resulting $p(I_z)$ distributions. To summarize this section, Eq. (E3) generates the exact unitary time evolution by simple matrix multiplication.

a. Quantum circuit

This unitary part of the evolution, $U_j = U_{\mathrm{act}} R_{-y}(\pi/2) U_{\mathrm{sense},j} R_x(\pi/2)$ is depicted as a quantum circuit in Fig. 1(b) of the main text. Specifically, we depict the action of U_j, where $\tau_j = 1/4A_{\mathrm{c}}$, on a pure nuclear state in the manifold $\{|I, I_z\rangle, |I, I_z \pm 1\rangle\}$. In this way $U_{\mathrm{sense},j}$ effectively becomes a Z rotation of the electron conditional on the nuclear polarization fluctuating one unit away from the lock point. Furthermore, by choosing a drive time $T = 2/A_{\mathrm{nc}}\sqrt{I(I+1)}$, the action of the U_{act} gate becomes an exact SWAP operation (around zero polarization, $I_z = 0$). These specific choices mean the quantum circuit depicts the limit cycle behavior at the ultimate limit of the cooling algorithm: fluctuations of a single unit are detected with a conditional electron rotation and corrected deterministically with a SWAP operation.

3. Adding nonunitary evolution

There are several nonunitary processes to include in our model, the first of which is necessary for the feedback algorithm, and the remainder are dephasing and relaxation processes that hamper feedback.

a. Electron reset

This nonunitary process crucial to the operation of feedback resets the state of the electron spin via incoherent spin pumping. We simulate this process with the following amplitude-damping channel [62] on the electron spin:

$$\mathcal{K}^{\mathrm{reset}}: \rho \to K_0^r \rho K_0^{r\dagger} + K_1^r \rho K_1^{r\dagger}, \tag{E5}$$

where the Kraus operators are defined as

$$K_0^r = \begin{pmatrix} 1 & 0 \\ 0 & 0 \end{pmatrix} \otimes \mathbb{1}_n, \qquad K_1^r = \begin{pmatrix} 0 & 1 \\ 0 & 0 \end{pmatrix} \otimes \mathbb{1}_n, \tag{E6}$$

and we have safely assumed unit fidelity spin pumping [63].

b. Transverse nuclear noise

In Appendix E 2 a we neglected the noncollinear term A_{nc} during sensing since including its effect explicitly in the $|S_z\rangle \otimes |I, I_z\rangle$ is computationally inefficient. Instead, we capture its effect on the dynamics by assuming I_x to be a zero-mean, classical Gaussian random variable $\mathcal{I}_x(t)$. This time-fluctuating transverse nuclear polarization induces broadening of the electronic energy levels, which results in electronic decoherence, that limits the cooling efficiency.

Within this model, the postsensing density operator is given by

$$\rho(\tau) = \langle U(\tau)\rho(0)U(\tau)^\dagger \rangle, \tag{E7}$$

where

$$U(\tau) = e^{-i\tau A_{\mathrm{c}} I_z S_z - i A_{\mathrm{nc}} \int_0^\tau dt' \mathcal{I}_x(dt') S_z}, \tag{E8}$$

and the averaging $\langle \cdots \rangle$ is done over all noise realizations through a path integral that commutes with the other operators in the evolution equation. The net effect of the evolution can be viewed as a coherence buildup due to the longitudinal polarization $A_{\mathrm{c}} I_z$, alongside decoherence due to the transverse noise $A_{\mathrm{nc}}\mathcal{I}_x$. Commuting with the collinear term, the noise imposes a transfer function $W(\tau)$ on electronic coherences [64], which we will now calculate.

We start from writing this transfer function explicitly:

$$W(\tau) = \langle e^{-i\int_0^\tau dt' A_{\mathrm{nc}} \mathcal{I}_x(t')} \rangle. \tag{E9}$$

Since the transverse polarization is a Gaussian random variable, the sum over all its realizations in time—labeled as X—is also a Gaussian random variable:

$$W(\tau) = \int_{-\infty}^{\infty} dX \frac{1}{\sqrt{2\pi}\sigma_\tau} e^{-X^2/2\sigma_\tau^2} e^{iX} = e^{-\sigma_\tau^2/2}. \tag{E10}$$

We can find σ_τ by taking (without loss of generality) $\langle X \rangle = 0$ and evaluating the autocorrelation function:

$$\sigma_\tau^2 = \langle X^2(\tau) \rangle = A_{\mathrm{nc}}^2 \int_0^\tau dt_1 \int_0^\tau dt_2 \langle \mathcal{I}_x(t_1)\mathcal{I}_x(t_2) \rangle. \tag{E11}$$

Assuming that the noise is stationary, this correlator is dependent only on $T = |t_1 - t_2|$, such that

$$\langle \mathcal{I}_x(t_1)\mathcal{I}_x(t_2)\rangle = \langle \mathcal{I}_x(T)\mathcal{I}_x(0)\rangle \quad \forall \; t_1, t_2. \tag{E12}$$

In line with previous works [65,66] we take the amplitude of this classical variable to be equal to the correlator of our simplified model:

$$\langle \mathcal{I}_x(T)\mathcal{I}_x(0)\rangle = e^{-\Gamma T/2}\cos(\omega_n T)\langle I_x(0)^2\rangle, \tag{E13}$$

where Γ is the rate of pure nuclear dephasing. Assuming $I_x(0)^2 = I_y(0)^2$, Eq. (E13) is equal to

$$\langle \mathcal{I}_x(T)\mathcal{I}_x(0)\rangle = \frac{1}{2}e^{-\Gamma T/2}\cos(\omega_n T)(I^2 - \langle I_z(0)^2\rangle). \tag{E14}$$

Putting this all together, we have

$$\sigma_\tau^2 = \frac{1}{2}(I^2 - \langle I_z(0)^2\rangle)A_{\mathrm{nc}}^2 \int_0^\tau dt_1 \int_0^\tau dt_2 e^{-\Gamma|t_1-t_2|/2}\cos\omega_n(t_1 - t_2) \tag{E15}$$

$$= (I^2 - \langle I_z(0)^2\rangle)A_{\mathrm{nc}}^2\left[\frac{\frac{\Gamma}{2}\tau}{\frac{\Gamma^2}{4}+\omega_n^2} - \frac{\Gamma\omega_n e^{-\Gamma\tau/2}\sin\omega_n\tau + (\frac{\Gamma^2}{4}-\omega_n^2)(1-e^{-\Gamma\tau/2}\cos\omega_n\tau)}{(\frac{\Gamma^2}{4}+\omega_n^2)^2}\right], \tag{E16}$$

where the second line is the result of a change of variables $T = t_1 - t_2$ such that $dt_2 = -dT$, and a straightforward double integral. Since we have access to I and $\langle I_z(0)^2\rangle$ throughout the simulations, we have everything required to calculate $W(\tau) = e^{-\sigma_\tau^2/2}$. Intuitively, we can see from Eq. (E16) that at short times one observes some revivals of coherence related to Larmor precession, and at long times the decay of coherence becomes exponential.

Incorporating the above decay of electronic coherences into our calculation is achieved via the an electronic phase-damping channel:

$$\mathcal{K}^{\mathrm{TN}}:\rho \to \sum_{i=0}^{2} K_i^{\mathrm{TN}}\rho K_i^{\mathrm{TN}\dagger}, \tag{E17}$$

where TN stands for transverse noise, and

$$\begin{aligned} K_0^{\mathrm{TN}} &= \sqrt{W(\tau)}\mathbb{1}_e \otimes \mathbb{1}_n, \\ K_1^{\mathrm{TN}} &= \sqrt{1-W(\tau)}|\downarrow\rangle\langle\uparrow| \otimes \mathbb{1}_n, \\ K_2^{\mathrm{TN}} &= \sqrt{1-W(\tau)}|\uparrow\rangle\langle\downarrow| \otimes \mathbb{1}_n. \end{aligned} \tag{E18}$$

c. Optically induced electron relaxation

When shining nonresonant light on our QD system there exists an optically induced electron spin relaxation at a power-dependent rate $\Gamma_{\mathrm{opt}} \propto \Omega$, likely the result of photo-activated charge noise in the device [45]. This relaxation has the largest effect during the actuate gate, where we illuminate the sample for a significant time. We incorporate this into the model with a generalized amplitude damping channel:

$$\mathcal{K}^{\mathrm{opt}}:\rho \to \sum_{i=0}^{2} K_i^{\mathrm{opt}}\rho K_i^{\mathrm{opt}\dagger}, \tag{E19}$$

where

$$\begin{aligned} K_0^{\mathrm{opt}} &= \begin{pmatrix} 1 & 0 \\ 0 & e^{\Gamma_{\mathrm{opt}}T/2} \end{pmatrix} \otimes \mathbb{1}_n, \\ K_1^{\mathrm{opt}} &= \begin{pmatrix} e^{\Gamma_{\mathrm{opt}}T/2} & 0 \\ 0 & 1 \end{pmatrix} \otimes \mathbb{1}_n, \\ K_2^{\mathrm{opt}} &= \begin{pmatrix} 0 & \sqrt{1-e^{\Gamma_{\mathrm{opt}}T}} \\ \sqrt{1-e^{\Gamma_{\mathrm{opt}}T}} & 0 \end{pmatrix} \otimes \mathbb{1}_n. \end{aligned} \tag{E20}$$

We measure this relaxation rate via a separate Rabi driving measurement as per previous work [45]. For $\Omega = 402$ MHz we measure this relaxation rate to be 23.6 MHz, which we can rescale linearly with Rabi frequency allowing us to fix $\Gamma_{\mathrm{opt}} = 1.7$ MHz during actuation.

d. Pure nuclear dephasing

In Appendix E 3 b we considered pure nuclear dephasing acting to damp transverse nuclear coherences that couple to the electron during sensing. The same nuclear dephasing processes, which arise from inhomogeneity in the quadrupolar coupling strength underpinning the noncollinear term and electron-mediated nuclear-nuclear spin coupling, are present during actuation. We include pure nuclear dephasing at a rate Γ, the same rate as in Appendix E 3 b, via a nuclear phase-damping channel in each I manifold:

$$\mathcal{K}^{\mathrm{PD}}:\ \rho \to \sum_{i=0}^{2I+1} K_i^{\mathrm{PD}} \rho K_i^{\mathrm{PD}\dagger}, \tag{E21}$$

where

$$\begin{aligned} K_0^{\mathrm{PD}} &= e^{-\Gamma T/4} \mathbb{1}_e \otimes \mathbb{1}_n, \\ K_i^{\mathrm{PD}} &= \sqrt{1-e^{-\Gamma T/2}} \mathbb{1}_e \otimes |I, i-I-1\rangle\langle I, i-I-1|, \quad i \neq 0. \end{aligned} \tag{E22}$$

4. Combined evolution

Having introduced all the individual ingredients that comprise the simulation, here we combine them into what constitutes a simulation of a single run of the feedback algorithm. To complete our quantum channel shorthand notation for the unitary gates, we define

$$\begin{aligned} \mathcal{U}_j^1 &: \rho \to U_{\mathrm{sense},j} R_x\left(\frac{\pi}{2}\right) \rho R_x\left(\frac{\pi}{2}\right)^\dagger U_{\mathrm{sense},j}^\dagger, \\ \mathcal{U}^2 &: \rho \to R_{-y}\left(\frac{\pi}{2}\right) \rho R_{-y}\left(\frac{\pi}{2}\right)^\dagger, \\ \mathcal{U}^3 &: \rho \to U_{\mathrm{act}} \rho U_{\mathrm{act}}^\dagger. \end{aligned} \tag{E23}$$

A simulation of a single run of the feedback algorithm then proceeds as

$$\rho_{j+1} = \mathcal{K}^{\mathrm{reset}} \mathcal{K}^{\mathrm{PD}} \mathcal{U}^3 \mathcal{K}^{\mathrm{opt}} \mathcal{U}^2 \mathcal{K}^{\mathrm{TN}} \mathcal{U}_j^1 \rho_j. \tag{E24}$$

As in the preparation part of our physical implementation, in simulations we increase the sensing time in each step τ_j linearly from $\tau_0 = 30$ ns to $\tau_{43} = \tau_{\max}$ over 44 runs of the fundamental feedback cycle [Eq. (E24)]. Since our experimental sequence repeats this preparation indefinitely (interleaved with the experiment for a duty cycle of 88%, cf. Fig. 8), we operate in steady state. To this end we repeat the simulated preparation (constituting 44 fundamental feedback cycles) twice. We find this is sufficient to go from initial to steady state.

5. Weighting I manifolds

We now have a complete description of how we simulate the feedback dynamics in a given I manifold; the last consideration to make is how we weight the results from each manifold to obtain the quantity of interest $p(I_z)$. The first step is to trace over the electron degrees of freedom as we are interested solely in the nuclear density matrix, as such ρ refers to the nuclei only. We can reexpress the $(2^N \times 2^N)$-dimensional total nuclear density operator in terms of the density matrices in individual, uncorrelated I manifolds ρ_I as

$$\rho = \bigoplus_{I=0}^{N/2} w_{I,N} \rho_I^{\oplus D_{I,N}}, \tag{E25}$$

where $\oplus$ stands for matrix block concatenation and $D_{I,N}$ is the degeneracy of an I manifold [10]:

$$D_{I,N} = \frac{N!(2I+1)}{(\frac{N}{2}-I)!(\frac{N}{2}+I+1)!}. \tag{E26}$$

The weighting factors $w_{I,N}$ can be found by considering the $T = \infty$ initial state for the simulations:

$$\begin{aligned} \rho_{T=\infty} &= \frac{1}{2^N} \mathbb{1}_{2^N} \\ &= \frac{1}{2^N} \bigoplus_{I=0}^{N/2} \Bigg(\underbrace{\sum_{I_z=-I}^{I} |I, I_z\rangle\langle I, I_z|}_{\mathbb{1}_{2I+1}} \Bigg)^{\oplus D_{I,N}} \\ &= \frac{1}{2^N} \bigoplus_{I=0}^{N/2} (2I+1) \rho_{I,T=\infty}^{\oplus D_{I,N}}. \end{aligned} \tag{E27}$$

Comparing $\rho_{I,T=\infty}$ [Eq. (E27)] to ρ_I [Eq. (E25)], we obtain $w_{I,N} = (2I+1)/2^N$. With this we have everything required to calculate the expectation value of an arbitrary observable A as

$$\mathrm{Tr}\rho A = \sum_{I=0}^{N/2} w_{I,N} D_{I,N} \mathrm{Tr}\rho_I A, \tag{E28}$$

which we use to extract the probability distribution of I_z:

$$p(I_z) = \sum_{I=0}^{N/2} w_{I,N} D_{I,N} \langle I, I_z|\rho_I|I, I_z\rangle. \tag{E29}$$

The weights defined as $w'_{I,N} = w_{I,N} D_{I,N}$ are difficult to compute on a desktop computer for $N > 30\,000$, and so we use the approximate form [44]:

$$w'_{I,N} \approx \frac{2^{5/2} I(2I+1)}{\sqrt{\pi} N^{3/2}} e^{-2I^2/N}. \tag{E30}$$

In Fig. 12 we compare this approximate form (yellow curve) to the exact result (purple dotted curve) for $N = 30\,000$, where the quantitative agreement is clear. We further plot the approximate result for $N = 49\,000$, as well as the weights for the $46I$ values used in the simulations (blue crosses) as discussed in Appendix E 1. Note than since we require the weights to sum to 1 we renormalize these 46 values while preserving their relative weight.

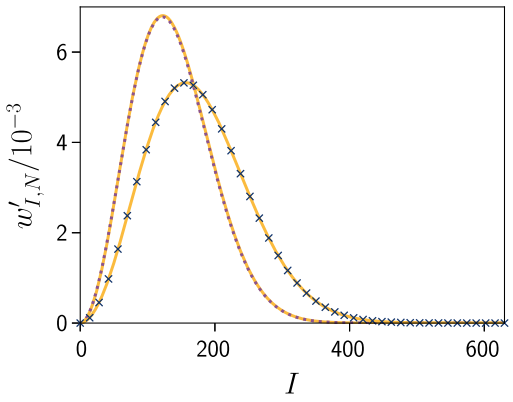

FIG. 12. Weighting factors for each I manifold. The purple dotted curve is the exact expression for the weights $w'_{I,N}$ for $N = 30\,000$, with the corresponding approximate version in yellow. We show only the latter for the case of $N = 49\,000$, overlaid with the 46 sampled points used in our simulations (blue crosses).

6. Fitting model to data

There are four free parameters in our model: A_c, A_{nc}, Γ, and an additional parameter ξ not yet discussed, which is the fraction of nuclei partaking in the magnon mode during actuation. This parameter is strongly motivated by previous work [37,38], where it was inferred from modeling that only a small fraction of the total N partake in coherent electron-nuclear exchange. This fraction ξ is included *ad hoc* as a scaling of $I \to \sqrt{\xi} I$ during the actuate gate, and thus scales the collective enhancement factor $f(I, I_z)$, which combined with A_{nc} sets the electron-nuclear coupling rate $\sim f(I, I_z) A_{nc}$. At the maximum degeneracy ($w_{I,N}$) point we have $f(I, I_z) \approx I = \sqrt{N/2}$, as such our scaling is conceptually equivalent to scaling $N \to \xi N$, during actuation only.

We get the first estimate of these four parameters from a least-squares fit of our model to the electron-nuclear exchange measurement of Fig. 3(c) of the main text. Specifically, we isolate the actuate step of our model, and extract the simulated ESR shift, $\Delta\omega = A_c \langle I_z \rangle$, versus T as per Eq. (E28). Fitting this simulated curve to the data fixes precisely $A_c = 0.63(2)$ MHz and $\Gamma = 6(2)$ MHz, which we then use in our feedback model. However, since ξ and A_{nc} are heavily coupled, this measurement only constrains the product $\sqrt{\xi N} A_{nc}$.

We then run our feedback simulation for each of the independent variables in the optimization curves of Figs. 3(a) and 3(c), extracting a T_2^* value at each point. We then manually search the 2D space $\{A_{nc}, \xi\}$ to match the two simulated optimization curves to the two datasets simultaneously. There is an optimum in this space since A_{nc} also strongly affects the transverse nuclear noise and in turn the attainable T_2^* values. As such only one set of $\{A_{nc}, \xi\}$ reproduces simultaneously the coherent coupling rate and the scale of T_2^*. After this manual search we fix ξ and perform a least-squares fit to obtain our best estimate of A_{nc} for this measurement. In conclusion, we obtain the fitted parameter set $A_c = 0.63(2)$ MHz, $\Gamma = 6(2)$ MHz, $\xi = 0.42$, and very similar A_{nc} values of 140(13) and 166(8) kHz for the exchange measurement and T_2^* optimization curves, respectively.

7. Modeling the ideal system

a. Optimization curves

The yellow curves of Fig. 13 are the result of our fitted simulation, extrapolated beyond the domain of the experimental data (black points). For the blue curve we simulate purely unitary evolution, i.e., $\Gamma_{opt} = \Gamma = 0$, and we neglect the transverse noise term $A_{nc} S_z I_x$. This latter consideration would be true of physical systems where a flip-flop actuator Hamiltonian could be engineered from a purely collinear hyperfine interaction. The other three colors represent simulations where we add one of the three sources of amplitude or phase damping present in our system to see the dominant effects (Appendices E 3 b–E 3 d).

Consider first the entirely unitary simulation (blue curve); strikingly we see oscillations in T_2^* at the nuclear

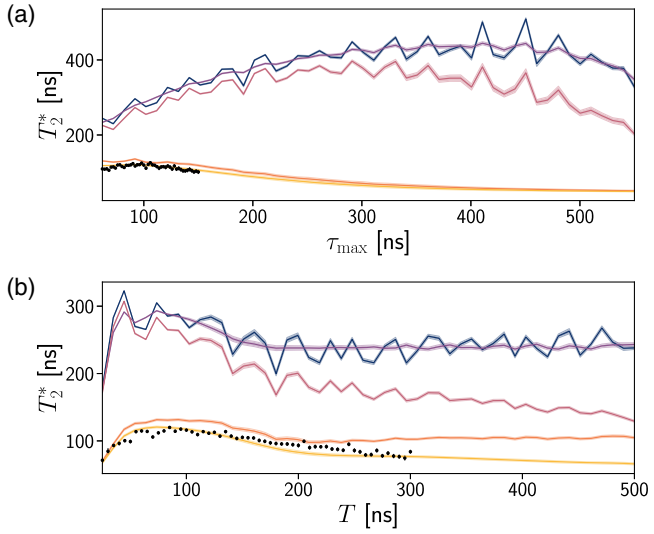

FIG. 13. Effects of relaxation and dephasing on feedback performance. (a),(b) T_2^* versus maximum sensing time τ_{max} and actuation time T, respectively. Black circles are the measured values (also shown in the main text, Fig. 3) with error bars representing the 68% confidence intervals. The solid curves are simulations of the data using the model parameters found in Appendix E 6, but where we include only one amplitude or phase-damping channel at a time. The blue curve is an entirely unitary quantum evolution, except for the explicit dissipative reset step. For the purple curve we include pure nuclear dephasing during actuation (Appendix E 3 d). For the pink curve we instead include optically induced electron relaxation (Appendix E 3 c). For the orange curve we include instead electron dephasing due to transverse noise during sensing (Appendix E 3 b). Lastly the yellow curve contains all three damping channels, and is the best-fit model included in the main text Fig. 3. Shaded regions represents the 68% confidence intervals.

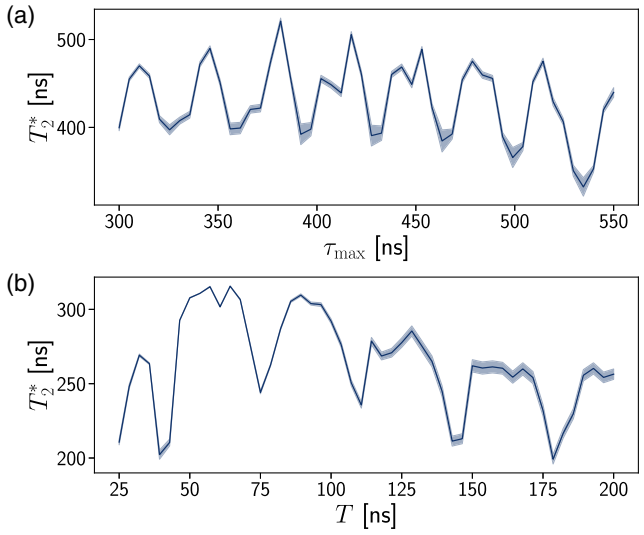

FIG. 14. Feedback performance for a single-species unitary algorithm. (a),(b) Simulated T_2^* versus maximum sensing time $\tau_{\max}$ and actuation time T, respectively. The evolution during the feedback algorithm is entirely unitary, except for the explicit dissipative reset step. Here we use the model parameters found in Appendix E 6, but we only simulate a single nuclear species with Zeeman frequency $\omega_n = 29$ MHz. Shaded regions represent the 68% confidence intervals.

Zeeman frequency in both the $\tau_{\max}$ and T dependence, which is due to the buildup of transverse nuclear coherences during feedback which then oscillate in the magnetic field. Since we have two species with different gyromagnetic ratios, these oscillations beat, resulting in what looks like high-frequency noise. To get a clearer physical picture, we plot the same simulation but for a single nuclear species in Fig. 14. The T dependence therein shows clearly that these high-frequency oscillations exist on top of a much lower-frequency, low-visibility oscillation corresponding to coherent electron-nuclear exchange. In the absence of any purification of I, as is the case in these simulations, the different exchange frequencies in different I manifolds alone combine to heavily damp the exchange. As such, even in the absence of dephasing, we only observe the first maximum in T_2^* versus T, which occurs at approximately 75 ns, in rough agreement with the π time measured in Fig. 2(d) of the main text. In the $\tau_{\max}$ dependence of Fig. 14 we see that behind the nuclear oscillations there is a broad optimum in sensing time around $\tau_{\max} \approx 400$ ns. This is entirely consistent with our intuition that feedback is best when we are sensitive to single-spin fluctuations, namely, $\tau_{\max} = 1/4A_c \approx 400$ ns.

Returning to Fig. 13, the first nonunitary process we consider is pure nuclear dephasing Γ during the actuate step (purple curves). Its main effect is that transverse coherences get damped sufficiently to remove the oscillations at the nuclear Zeeman frequency, smoothing the dependencies. This pure dephasing also contributes to the finite actuate gate fidelity, along with optically induced electron relaxation Γ_{opt}. The pink curves of Fig. 13 result from a simulation where we add this relaxation to the unitary case. From this we can see that even the modest actuate gate fidelity of 77% (Appendix B 3) does not modify the optimum performance greatly. Its predominant effect is on the T dependence, whereby it reduces the maximum T_2^* achievable and slightly reduces the optimum exchange time thanks to driven diffusion, as discussed in the main text.

Finally, the process which has the most marked effect on the performance of our feedback algorithm is the dephasing introduced by transverse noise during sensing, which we add to the unitary simulation to obtain the orange curves of Fig. 13. Optimum feedback is now a competition between minimizing the effect of transverse noise and maximizing sensitivity to spin fluctuations, reducing the optimal $\tau_{\max}$ and the maximum T_2^* attainable.

b. Purifying down to single quanta

In Fig. 15, we report the result of a simulation of our quantum-algorithmic feedback as applied to an ideal system, where all dephasing and damping rates have been set to zero. We plot $p(A_c\Delta I_z)$ versus $A_c\Delta I_z$ for the physical parameters found in Appendix E 6 and for the experimental parameters that lead to optimal purification, as quantified by T_2^*; namely, $\Omega = 29$ MHz, $T = 86$ ns, and $\tau_{\max} = 450$ ns. The resulting T_2^* is 510 ns, but most strikingly we see that the nuclear state is purified to a single macrostate I_z to within fluctuations of one quantum, $\Delta I_z = \pm 1$.

8. Nuclear Schrödinger cat state protocol

Herein we detail a simple extension to our algorithmic feedback protocol that allows for the generation of certain quantum states of the nuclear ensemble. Specifically, we generate Schrödinger kitten states, which we define as

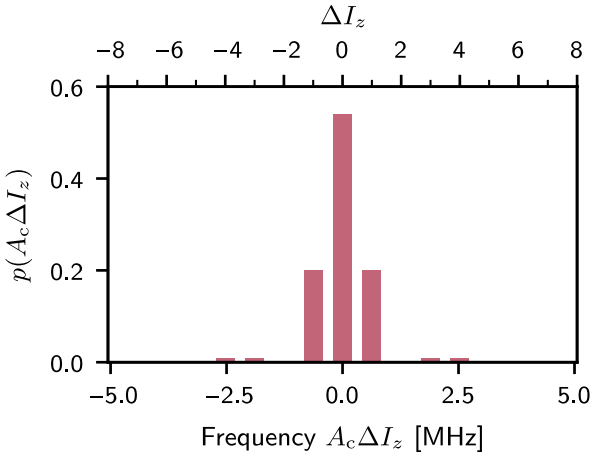

FIG. 15. Optimally purified state in the ideal case. $p(A_c\Delta I_z)$ versus $A_c\Delta I_z$ for the parameters found in Appendix E 6. With all dephasing and damping rates set to zero, we model the ideal system under optimal purification, which occurs at $\Omega = 29$ MHz, $T = 86$ ns, and $\tau_{\max} = 450$ ns. The system is purified to a single macrostate I_z to within fluctuations of a single quantum, i.e., $\Delta I_z = \pm 1$. We plot only a small range of ΔI_z, since the total probability outside this range is negligible.

superpositions of two collective states with small nuclear polarization, in analogy with coherent optical states with small amplitude [57]. This is made possible since our algorithm is entirely coherent except for the explicit dissipation operation on the electron. In general, the actuate gate generates electron-nuclear coherences. It is the dissipative reset step that prevents the proliferation of quantum coherences as the algorithm cycles. Any extension to our algorithm that seeks to generate quantum states of the nuclei must therefore map electron-nuclear coherences to the nuclear part of Hilbert space prior to reset.

Figure 16(a) presents a concrete example of such an extension. Suppose we start in a pure nuclear state $|I, I_z\rangle$. Our unmodified algorithm is designed for the purification of I_z and, while not fully elucidated theoretically, feedback applied to optically active quantum dots has been found to also produce a weak purification in I. This I purification

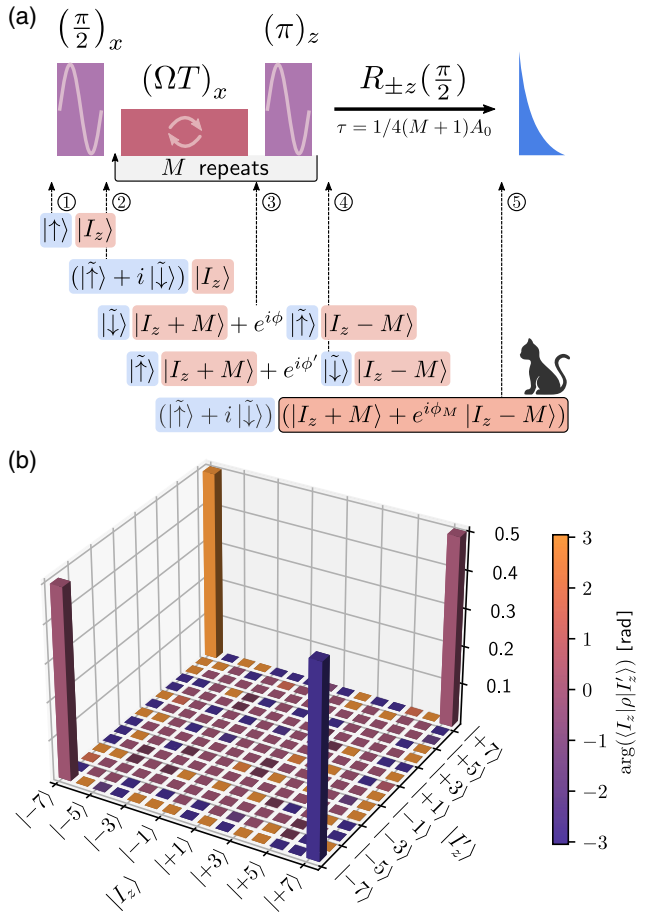

FIG. 16. Simulating Schrödinger kitten-state generation. (a) A copy of Fig. 5 of the main text. Pulse sequence representing the proposed kitten-state protocol. Square pulses depict coherent qubit control pulses. The blue shape represents dissipative reset of the electron. We write down the electron-nuclear state at each step. (b) Representation of the final density matrix ρ after the protocol, with $M = 7$, is applied in the $I = 7$ manifold of nuclear states. The electron has been traced out of the density matrix. The height and color of each bar represent the absolute value and argument of each matrix element, respectively.

can be witnessed as dark-state correlations of the ensemble [41,48,67]. Impurity in I or I_z will limit the fidelity of the nuclear state we can prepare using the protocol proposed below. That said, for clarity, we take a pure initial state, $|\uparrow\rangle|I, I_z\rangle$, and omit I in our notation henceforth, as it is unchanged by the protocol.

The first part of the modified protocol is simply the sense and actuate step of our feedback algorithm, which generates the electron-nuclear entangled state, $|\tilde{\downarrow}\rangle|I_z + 1\rangle + e^{i\phi}|\tilde{\uparrow}\rangle|I_z - 1\rangle$ (where proper normalization is implied hereupon). Note that the phase ϕ results from the diagonal part of the actuate Hamiltonian $H^0_{\text{act}} = \Omega S_x + \omega_n I_z$, in the eigenbasis of S_x, i.e., $\{|\tilde{\uparrow}\rangle, |\tilde{\downarrow}\rangle\}$. The first modification from the original feedback algorithm is an unconditional electronic $R_z(\pi)$ rotation immediately after the actuate gate. This allows us to repeat the actuate and $R_z(\pi)$ gates M times, which does nothing to the degree of electron-nuclear coherence, but pushes the coherences out to higher nuclear polarization, i.e., $|\tilde{\uparrow}\rangle|I_z + M\rangle + e^{i\phi'}|\tilde{\downarrow}\rangle|I_z - M\rangle$.

The second, crucial extension to the feedback algorithm is then a disentangling gate, which is the wait time depicted in Fig. 16(a). Selecting the appropriate wait time, $\tau = 1/4(M+1)A_0$, leads to a $R_{\pm z}(\pi/2)$ rotation conditional on the sign of nuclear polarization, yielding the separable state $(|\tilde{\uparrow}\rangle + i|\tilde{\downarrow}\rangle)(|I_z + M\rangle + e^{i\phi_M}|I_z - M\rangle)$. Finally, the reset step polarizes the electron, while preserving the purely nuclear coherences, thus preventing the electron from becoming reentangled with the nuclei. Since the states $|I, I_z \pm M\rangle$ are collective states of the entire ensemble, a quantum superposition thereof constitutes a Schrödinger kitten state [57].

For completeness, we note that as the nuclear state is pushed out in polarization, the actuation time required to achieve the SWAP operation must be chosen as $T = 2/A_{\text{nc}}\sqrt{I(I+1) - M(M-1)}$ (assuming the initial state for the protocol is the zero-polarization state $|I, 0\rangle$). In Fig. 16(b), we present the result of a simulation of the proposed kitten-state protocol, for $M = 7$, operating in the nuclear Hilbert space spanned by $I = 7, I_z \in \{I, I-1, \ldots, -I\}$. We capture the essence of this extension to our feedback algorithm by simulating purely unitary evolution, using the methods described in Appendix E 2. As expected, the final density matrix ρ features nuclear coherences, albeit with an arbitrary but known phase ϕ_M, between $|I_z = +7\rangle$ and $|I_z = -7\rangle$, confirming the quantum nature of the superposition.

[1] C. Monroe, W. C. Campbell, L.-M. Duan, Z.-X. Gong, A. V. Gorshkov, P. W. Hess, R. Islam, K. Kim, N. M. Linke, G. Pagano, P. Richerme, C. Senko, and N. Y. Yao, *Programmable Quantum Simulations of Spin Systems with Trapped Ions*, Rev. Mod. Phys. **93**, 025001 (2021).

[2] D. A. Abanin, E. Altman, I. Bloch, and M. Serbyn, *Colloquium: Many-Body Localization, Thermalization, and Entanglement*, Rev. Mod. Phys. **91**, 021001 (2019).

[3] T. H. Taminiau, J. Cramer, T. Van Der Sar, V. V. Dobrovitski, and R. Hanson, *Universal Control and Error Correction in Multi-Qubit Spin Registers in Diamond*, Nat. Nanotechnol. **9**, 171 (2014).

[4] S. Debnath, N. M. Linke, C. Figgatt, K. A. Landsman, K. Wright, and C. Monroe, *Demonstration of a Small Programmable Quantum Computer with Atomic Qubits*, Nature (London) **536**, 63 (2016).

[5] A. Omran, H. Levine, A. Keesling, G. Semeghini, T. T. Wang, S. Ebadi, H. Bernien, A. S. Zibrov, H. Pichler, S. Choi, J. Cui, M. Rossignolo, P. Rembold, S. Montangero, T. Calarco, M. Endres, M. Greiner, V. Vuletić, and M. D. Lukin, *Generation and Manipulation of Schrödinger Cat States in Rydberg Atom Arrays*, Science **365**, 570 (2019).

[6] E. A. Chekhovich, S. F. da Silva, and A. Rastelli, *Nuclear Spin Quantum Register in an Optically Active Semiconductor Quantum Dot*, Nat. Nanotechnol. **15**, 999 (2020).

[7] J. M. Taylor, C. M. Marcus, and M. D. Lukin, *Long-Lived Memory for Mesoscopic Quantum Bits*, Phys. Rev. Lett. **90**, 206803 (2003).

[8] E. V. Denning, D. A. Gangloff, M. Atatüre, J. Mørk, and C. Le Gall, *Collective Quantum Memory Activated by a Driven Central Spin*, Phys. Rev. Lett. **123**, 140502 (2019).

[9] C. E. Bradley, J. Randall, M. H. Abobeih, R. C. Berrevoets, M. J. Degen, M. A. Bakker, M. Markham, D. J. Twitchen, and T. H. Taminiau, *A Ten-Qubit Solid-State Spin Register with Quantum Memory Up to One Minute*, Phys. Rev. X **9**, 031045 (2019).

[10] R. H. Dicke, *Coherence in Spontaneous Radiation Processes*, Phys. Rev. **93**, 99 (1954).

[11] Z. Wang, H. Li, W. Feng, X. Song, C. Song, W. Liu, Q. Guo, X. Zhang, H. Dong, D. Zheng, H. Wang, and D.-W. Wang, *Controllable Switching between Superradiant and Subradiant States in a 10-qubit Superconducting Circuit*, Phys. Rev. Lett. **124**, 013601 (2020).

[12] S. Choi, J. Choi, R. Landig, G. Kucsko, H. Zhou, J. Isoya, F. Jelezko, S. Onoda, H. Sumiya, V. Khemani, C. von Keyserlingk, N. Y. Yao, E. Demler, and M. D. Lukin, *Observation of Discrete Time-Crystalline Order in a Disordered Dipolar Many-Body System*, Nature (London) **543**, 221 (2017).

[13] J. Zhang, P. W. Hess, A. Kyprianidis, P. Becker, A. Lee, J. Smith, G. Pagano, I.-D. Potirniche, A. C. Potter, A. Vishwanath, N. Y. Yao, and C. Monroe, *Observation of a Discrete Time Crystal*, Nature (London) **543**, 217 (2017).

[14] W. D. Phillips, *Nobel Lecture: Laser Cooling and Trapping of Neutral Atoms*, Rev. Mod. Phys. **70**, 721 (1998).

[15] D. J. Wineland, R. E. Drullinger, and F. L. Walls, *Radiation-Pressure Cooling of Bound Resonant Absorbers*, Phys. Rev. Lett. **40**, 1639 (1978).

[16] C. Monroe, D. M. Meekhof, B. E. King, S. R. Jefferts, W. M. Itano, D. J. Wineland, and P. Gould, *Resolved-Sideband Raman Cooling of a Bound Atom to the 3D Zero-Point Energy*, Phys. Rev. Lett. **75**, 4011 (1995).

[17] H. J. Lee, C. S. Adams, M. Kasevich, and S. Chu, *Raman Cooling of Atoms in an Optical Dipole Trap*, Phys. Rev. Lett. **76**, 2658 (1996).

[18] A. Urvoy, Z. Vendeiro, J. Ramette, A. Adiyatullin, and V. Vuletić, *Direct Laser Cooling to Bose-Einstein Condensation in a Dipole Trap*, Phys. Rev. Lett. **122**, 203202 (2019).

[19] M. D. LaHaye, O. Buu, B. Camarota, and K. C. Schwab, *Approaching the Quantum Limit of a Nanomechanical Resonator*, Science **304**, 74 (2004).

[20] J. D. Teufel, T. Donner, D. Li, J. W. Harlow, M. S. Allman, K. Cicak, A. J. Sirois, J. D. Whittaker, K. W. Lehnert, and R. W. Simmonds, *Sideband Cooling of Micromechanical Motion to the Quantum Ground State*, Nature (London) **475**, 359 (2011).

[21] S. Gröblacher, J. B. Hertzberg, M. R. Vanner, G. D. Cole, S. Gigan, K. C. Schwab, and M. Aspelmeyer, *Demonstration of an Ultracold Micro-optomechanical Oscillator in a Cryogenic Cavity*, Nat. Phys. **5**, 485 (2009).

[22] S. O. Valenzuela, W. D. Oliver, D. M. Berns, K. K. Berggren, L. S. Levitov, and T. P. Orlando, *Microwave-Induced Cooling of a Superconducting Qubit*, Science **314**, 1589 (2006).

[23] J. Zhang, Y. xi Liu, R. B. Wu, K. Jacobs, and F. Nori, *Quantum Feedback: Theory, Experiments, and Applications*, Phys. Rep. **679**, 1 (2017).

[24] G. Franklin, *Feedback Control of Dynamic Systems* (Prentice-Hall, Upper Saddle River, NJ, 2002).

[25] H. M. Wiseman, *Quantum Measurement and Control* (Cambridge University Press, Cambridge, England, 2010).

[26] J. Wang and H. M. Wiseman, *Feedback-Stabilization of an Arbitrary Pure State of a Two-Level Atom*, Phys. Rev. A **64**, 063810 (2001).

[27] A. Vinante and P. Falferi, *Feedback-Enhanced Parametric Squeezing of Mechanical Motion*, Phys. Rev. Lett. **111**, 207203 (2013).

[28] X. Zhou, I. Dotsenko, B. Peaudecerf, T. Rybarczyk, C. Sayrin, S. Gleyzes, J. M. Raimond, M. Brune, and S. Haroche, *Field Locked to a Fock State by Quantum Feedback with Single Photon Corrections*, Phys. Rev. Lett. **108**, 243602 (2012).

[29] K. C. Cox, G. P. Greve, J. M. Weiner, and J. K. Thompson, *Deterministic Squeezed States with Collective Measurements and Feedback*, Phys. Rev. Lett. **116**, 093602 (2016).

[30] S. Lloyd, *Coherent Quantum Feedback*, Phys. Rev. A **62**, 022108 (2000).

[31] S. Iida, M. Yukawa, H. Yonezawa, N. Yamamoto, and A. Furusawa, *Experimental Demonstration of Coherent Feedback Control on Optical Field Squeezing*, IEEE Trans. Autom. Control **57**, 2045 (2012).

[32] R. J. Nelson, Y. Weinstein, D. Cory, and S. Lloyd, *Experimental Demonstration of Fully Coherent Quantum Feedback*, Phys. Rev. Lett. **85**, 3045 (2000).

[33] M. Hirose and. Cappellaro, *Coherent Feedback Control of a Single Qubit in Diamond*, Nature (London) **532**, 77 (2016).

[34] H. Bluhm, S. Foletti, D. Mahalu, V. Umansky, and A. Yacoby, *Enhancing the Coherence of a Spin Qubit by Operating It as a Feedback Loop That Controls Its Nuclear Spin Bath*, Phys. Rev. Lett. **105**, 216803 (2010).

[35] C. Latta, A. Högele, Y. Zhao, A. N. Vamivakas, P. Maletinsky, M. Kroner, J. Dreiser, I. Carusotto, A. Badolato, D. Schuh, W. Wegscheider, M. Atature, and A. Imamoglu, *Confluence of Resonant Laser Excitation and Bidirectional Quantum-Dot Nuclear-Spin Polarization*, Nat. Phys. **5**, 758 (2009).

[36] G. Éthier-Majcher, D. Gangloff, R. Stockill, E. Clarke, M. Hugues, C. Le Gall, and M. Atatüre, *Improving a Solid-State Qubit through an Engineered Mesoscopic Environment*, Phys. Rev. Lett. **119**, 130503 (2017).

[37] D. A. Gangloff, G. Éthier-Majcher, C. Lang, E. V. Denning, J. H. Bodey, D. M. Jackson, E. Clarke, M. Hugues, C. Le Gall, and M. Atatüre, *Quantum Interface of an Electron and a Nuclear Ensemble*, Science **364**, 62 (2019).

[38] D. M. Jackson, D. A. Gangloff, J. H. Bodey, L. Zaporski, C. Bachorz, E. Clarke, M. Hugues, C. Le Gall, and M. Atatüre, *Quantum Sensing of a Coherent Single Spin Excitation in a Nuclear Ensemble*, Nat. Phys. **17**, 585 (2021).

[39] X. Xu, W. Yao, B. Sun, D. G. Steel, A. S. Bracker, D. Gammon, and L. J. Sham, *Optically Controlled Locking of the Nuclear Field via Coherent Dark-State Spectroscopy*, Nature (London) **459**, 1105 (2009).

[40] W. Yang and L. J. Sham, *General Theory of Feedback Control of a Nuclear Spin Ensemble in Quantum Dots*, Phys. Rev. B **88**, 235304 (2013).

[41] J. M. Taylor, A. Imamoglu, and M. D. Lukin, *Controlling a Mesoscopic Spin Environment by Quantum Bit Manipulation*, Phys. Rev. Lett. **91**, 246802 (2003).

[42] W. Chen, J. Hu, Y. Duan, B. Braverman, H. Zhang, and V. Vuletić, *Carving Complex Many-Atom Entangled States by Single-Photon Detection*, Phys. Rev. Lett. **115**, 250502 (2015).

[43] B. Urbaszek, X. Marie, T. Amand, O. Krebs, P. Voisin, P. Maletinsky, A. Högele, and A. Imamoglu, *Nuclear Spin Physics in Quantum Dots: An Optical Investigation*, Rev. Mod. Phys. **85**, 79 (2013).

[44] G. G. Kozlov, *Exactly Solvable Spin Dynamics of an Electron Coupled to a Large Number of Nuclei; The Electron-Nuclear Spin Echo in a Quantum Dot*, J. Exp. Theor. Phys. **105**, 803 (2007).

[45] J. H. Bodey, R. Stockill, E. V. Denning, D. A. Gangloff, G. Éthier-Majcher, D. M. Jackson, E. Clarke, M. Hugues, C. L. Gall, and M. Atatüre, *Optical Spin Locking of a Solid-State Qubit*, npj Quantum Inf. **5**, 95 (2019).

[46] C.-W. Huang and X. Hu, *Theoretical Study of Nuclear Spin Polarization and Depolarization in Self-Assembled Quantum Dots*, Phys. Rev. B **81**, 205304 (2010).

[47] A. Högele, M. Kroner, C. Latta, M. Claassen, I. Carusotto, C. Bulutay, and A. Imamoglu, *Dynamic Nuclear Spin Polarization in the Resonant Laser Excitation of an InGaAs Quantum Dot*, Phys. Rev. Lett. **108**, 197403 (2012).

[48] D. A. Gangloff, L. Zaporski, J. H. Bodey, C. Bachorz, D. M. Jackson, G. Éthier-Majcher, C. Lang, E. Clarke, M. Hugues, C. Le Gall, and M. Atatüre, *Witnessing Quantum Correlations in a Nuclear Ensemble via an Electron Spin Qubit*, Nat. Phys. **17**, 1247 (2021).

[49] C. L. Degen, F. Reinhard, and P. Cappellaro, *Quantum Sensing*, Rev. Mod. Phys. **89**, 035002 (2017).

[50] S. R. Hartmann and E. L. Hahn, *Nuclear Double Resonance in the Rotating Frame*, Phys. Rev. **128**, 2042 (1962).

[51] A. Henstra and W. Wenckebach, *The Theory of Nuclear Orientation via Electron Spin Locking (NOVEL)*, Mol. Phys. **106**, 859 (2008).

[52] D. K. Park, N. A. Rodriguez-Briones, G. Feng, R. Rahimi, J. Baugh, and R. Laflamme, *Heat Bath Algorithmic Cooling with Spins: Review and Prospects*, *Electron Spin Resonance (ESR) Based Quantum Computing* (Springer, New York, 2016).

[53] G. Gillard, I. M. Griffiths, G. Ragunathan, A. Ulhaq, C. McEwan, E. Clarke, and E. A. Chekhovich, *Fundamental Limits of Electron and Nuclear Spin Qubit Lifetimes in an Isolated Self-Assembled Quantum Dot*, npj Quantum Inf. **7**, 43 (2021).

[54] A. R. Onur and C. H. Van Der Wal, *Two-Laser Dynamic Nuclear Polarization with Semiconductor Electrons: Feedback, Suppressed Fluctuations, and Bistability Near Two-Photon Resonance*, Phys. Rev. B **98**, 165304 (2018).

[55] L. Zaporski, N. Shofer, J. H. Bodey, S. Manna, G. Gillard, D. M. Jackson, M. H. Appel, C. Schimpf, S. C. da Silva, J. Jarman, G. Delamare, G. Park, U. Haeusler, E. A. Chekhovich, A. Rastelli, D. A. Gangloff, M. Atatüre, and C. Le Gall, *Ideal Refocusing of an Optically Active Spin Qubit under Strong Hyperfine Interactions*, arXiv:2206.01223.

[56] R. Stockill, C. Le Gall, C. Matthiesen, L. Huthmacher, E. Clarke, M. Hugues, and M. Atatüre, *Quantum Dot Spin Coherence Governed by a Strained Nuclear Environment*, Nat. Commun. **7**, 12745 (2016).

[57] A. Ourjoumtsev, R. Tualle-Brouri, J. Laurat, and P. Grangier, *Generating Optical Schrödinger Kittens for Quantum Information Processing*, Science **312**, 83 (2006).

[58] D. D. Awschalom, R. Hanson, J. Wrachtrup, and B. B. Zhou, *Quantum Technologies with Optically Interfaced Solid-State Spins*, Nat. Photonics **12**, 516 (2018).

[59] L. Huthmacher, R. Stockill, E. Clarke, M. Hugues, C. Le Gall, and M. Atatüre, *Coherence of a Dynamically Decoupled Quantum-Dot Hole Spin*, Phys. Rev. B **97**, 241413(R) (2018).

[60] C. Latta, A. Srivastava, and A. Imamoğlu, *Hyperfine Interaction-Dominated Dynamics of Nuclear Spins in Self-Assembled InGaAs Quantum Dots*, Phys. Rev. Lett. **107**, 167401 (2011).

[61] G. Wüst, M. Munsch, F. Maier, A. V. Kuhlmann, A. Ludwig, A. D. Wieck, D. Loss, M. Poggio, and R. J. Warburton, *Role of the Electron Spin in Determining the Coherence of the Nuclear Spins in a Quantum Dot*, Nat. Nanotechnol. **11**, 885 (2016).

[62] M. A. Nielsen and I. L. Chuang, *Quantum Computation and Quantum Information* (Cambridge University Press, Cambridge, England, 2019).

[63] M. Atatüre, J. Dreiser, A. Badolato, A. Högele, K. Karrai, and A. Imamoglu, *Quantum-Dot Spin-State Preparation with Near-Unity Fidelity*, Science **312**, 551 (2006).

[64] Ł. Cywiński, R. M. Lutchyn, C. P. Nave, and S. Das Sarma, *How to Enhance Dephasing Time in Superconducting Qubits*, Phys. Rev. B **77**, 174509 (2008).

[65] H. Bluhm, S. Foletti, I. Neder, M. Rudner, D. Mahalu, V. Umansky, and A. Yacoby, *Dephasing Time of GaAs Electron-Spin Qubits Coupled to a Nuclear Bath Exceeding* 200 μs, Nat. Phys. **7**, 109 (2011).

[66] T. Botzem, R. P. G. McNeil, J.-M. Mol, D. Schuh, D. Bougeard, and H. Bluhm, *Quadrupolar and Anisotropy Effects on Dephasing in Two-Electron Spin Qubits in GaAs*, Nat. Commun. **7**, 11170 (2016).

[67] H. Christ, J. I. Cirac, and G. Giedke, *Quantum Description of Nuclear Spin Cooling in a Quantum Dot*, Phys. Rev. B **75**, 155324 (2007).